

NASA Contractor Report 3208

NASA
CR
3208
c.1

LOAN COPY: RETURN
AFWL TECHNICAL LIBRARY
KIRTLAND AFB, N. M.

0061758



TECH LIBRARY KAFB, NM

A Three Dimensional Vortex Wake Model for Missiles at High Angles of Attack

J. Steven Sheffield and F. D. Deffenbaugh

CONTRACT NAS2-9579
JANUARY 1980

NASA



NASA Contractor Report 3208

A Three Dimensional Vortex Wake Model for Missiles at High Angles of Attack

J. Steven Sheffield and F. D. Deffenbaugh
TRW Defense and Space Systems Group
Redondo Beach, California

Prepared for
Ames Research Center
under Contract NAS2-9579



National Aeronautics
and Space Administration

**Scientific and Technical
Information Office**

1980

TABLE OF CONTENTS

NOTATION	iv
SUMMARY	1
CHAPTER 1. INTRODUCTION	2
1.1 Background	2
1.2 Model Objectives	4
CHAPTER 2. SOLUTION METHOD	6
2.1 Potential Solution	6
2.2 Straight Vortex Model	7
2.3 Segmented Vortex Model	8
2.4 Curved Vortex Model	9
CHAPTER 3. MODEL EVALUATION	10
3.1 Potential Assumption	11
3.2 Vortex Parameters	12
3.3 Positioning Algorithm	13
3.4 Singularity Cutoff	14
CHAPTER 4. VORTEX POSITIONS	16
4.1 Straight Vortex Positions.	16
4.2 Curved Vortex Positions	16
4.3 Elliptic Nose	17
CHAPTER 5. BODY FORCES AND LOAD DISTRIBUTION	19
5.1 Variation of C_N and C_Y with α	19
5.2 Cutoff Sensitivity	19
5.3 Side Load Distribution	20

	Page
CHAPTER 6. DISCUSSION AND CONCLUSIONS	21
APPENDIX-VORTEX INDUCED VELOCITIES	23
REFERENCES	26
FIGURES	28

NOTATION

A_b	base area of body
C_N	normal force coefficient = $\frac{\text{normal force}}{q_\infty A_b}$
c_n	local normal force coefficient per unit length divided by fineness ratio
C_p	pressure coefficient = $\frac{p-p_\infty}{q_\infty}$
C_Y	side force coefficient = $\frac{\text{side force}}{q_\infty A_b}$
c_y	local side force coefficient per unit length divided by fineness ratio
d	body cross section diameter or for bodies with non-circular cross section = $\frac{2\sqrt{A_b}}{\pi}$
f	fineness ratio = ℓ/d
ℓ	body length
ℓ_i	vortex segment length
M	free stream Mach number
R_c	radius of curvature of circular arc connecting three adjacent vortex segment endpoints
r_c	assumed radius for vortex core for self-induced velocity calculations
Re	Reynolds number based on a one foot length scale in the MX wind tunnel tests
\bar{U}_∞	free stream velocity vector
\bar{U}_v	vortex induced velocity vector
\bar{U}_v^i	velocity vector induced by a single vortex segment or ray

NOTATION (CONTINUED)

x, X	axial distance along body centerline scaled by body length
y, Y	distance above body centerline in angle of attack plane scaled by body length
z, Z	distance from body centerline measured normal to x and y axes and scaled by body length
α	angle of attack
Γ	vortex strength scaled by body length and free stream velocity
ϵ	integral cutoff distance in self-induced vortex velocity
ξ	asymptotic angle of vortex to body centerline
σ	source density strength
ϕ	roll angle of velocity potential
χ	vortex direction parameter = $\tan \xi / \tan \alpha$

A THREE DIMENSIONAL VORTEX WAKE MODEL
FOR MISSILES AT HIGH ANGLES OF ATTACK

by

J. Steven Sheffield and F. D. Deffenbaugh

TRW Systems and Energy, Inc.

SUMMARY

A three dimensional model for the steady flow past missile and aircraft nose shaped bodies is presented based on augmenting a potential solution with a wake composed of vortex filaments. The vortex positions are determined by the requirement that they in some sense align with the flow. The aerodynamic loads on the body are compared with experimental values and used to evaluate the model.

The vortex positions compare well with flow visualization results for slender bodies at high angles of attack. The approximations in the wake near the body cause peaks in the force distributions more severe than in the measured values.

For given vortex strengths and body attachment points multiple steady vortex positions were not found.

CHAPTER 1. INTRODUCTION

The vortex wake which develops due to separated flow over missiles and aircraft noses at high angle of attack results in augmented lift and side forces unpredicted by slender body theory. Wind tunnel investigations have revealed that a variety of vortex formations can develop for variations in angle of attack, flow conditions and body geometry. Seemingly slight changes in configuration such as rolling the model can result in the side force changing magnitude and even direction.

Examining a simple model for the possible vortex wake configurations and the relation between those configurations and the forces on the body could help the understanding of the physical phenomenon responsible for these experimental results.

1.1 Background

Much of the work examining the wake behind bodies of revolution has been based on the crossflow analogy, replacing the steady three dimensional problem with a time dependent, two dimensional one. Thompson and Morrison (1) suggested that the wake in the crossflow plane be modeled using a Karman vortex street. In their experiments with slender cone cylinders, the wake behavior could be correlated over a large range of Mach number and angle of attack using crossflow Karman vortex street relations. They found that a combination of the sweepback principle with the vortex street theory, requiring the vortex street velocity to be cancelled by the component of the freestream velocity normal to the vortex lines provided reasonable estimates for the experimentally measured vortex strength.

A number of investigators have since developed predictive techniques using Karman vortex street theory. The required empirical input is often the Thompson and Morrison correlations. Fidler (2), Kubin (3), and Kao (4) all use this approach with minor variations to account for the nose vortices which do not follow the pattern of the Karman vortex street.

A somewhat less empirical approach involves the lumped vortex crossflow model, initially suggested by Bryson in Reference 5. In this model a

potential point vortex is joined to the cylinder by a feeding sheet of negligible strength. The strength and motion of the vortex is found by requiring the force on each point vortex to balance the force on the vortex sheet. The force per unit length on the body cross section is equal to the time rate of change of momentum in the crossflow plane. Schindel (6) extended Bryson's model to include elliptic cross sections; Wardlaw (7) used the same technique for asymmetric vortices.

The most recent models of the wake are those which replace Bryson's feeding sheet with a number of free point vortices which are allowed to roll up to form a concentrated vortex. Angelucci (8) and Marshall and Deffenbaugh (9) used this model for symmetric shedding. Wardlaw (10) and Deffenbaugh (11) have extended the work to include asymmetric vortex development. Angelucci calculates the force distribution using the vortex impulse theorem. Wardlaw uses a momentum balance similar to Bryson. Marshall and Deffenbaugh calculate the circumferential pressure distribution and obtain the forces by pressure integration. In the approach used by Marshall and Deffenbaugh, the boundary layer is solved for numerically, which eliminates the need to specify the separation points empirically as in all the other flow field models, and secondary vortex formation is accounted for. The backflow induced secondary vortex formation must be accounted for to determine the proper vortex wake structure and pressure distribution.

Experimental investigators have attempted to identify the wake structure with the resulting loads on the bodies. The vortex structure has been examined by several visualization and measurement methods. Jorgensen (12) used the vapor-screen technique to identify the vortex formation at several stations along the body and oil-flow photographs to examine the flow patterns on the surfaces of the bodies. Force measurements are taken on many of the same bodies. Clark (13) and Spangler and Mendenhall (14) used air bubbles in water tunnel experiments to identify the vortices, laser-Doppler anemometer measurements for the flow velocities and internal strain gages to measure forces and moments on the structure. The velocity measurements can be integrated to estimate the vortex strength to go along with the measured vortex positions and body forces.

The MX wind tunnel tests (11 and 15-18) measured pressure on the body and surveyed the wake using a rake probe. The body pressures can be integrated to give force distributions associated with the probe measured wake structure. In the work of Thompson and Morrison schlieren photographs were used to determine vortex positions and Pitot pressure measurements to estimate the flow velocities and resulting vortex strengths. Laser Doppler velocimeter measurements have been used by Owen and Johnson (19) and Yanta and Wardlaw (20) to determine the wake flow in crossflow planes. From the velocity profiles the vortex position and strengths can be determined.

The experimental work has identified vortex asymmetries which appear in conjunction with asymmetric loads on the body. However, a range of value for the side force are obtained for slight changes in configurations. Figure 1 shows the variation in the side load distribution with roll angle on a slightly blunted ogive cylinder from the MX tests. These variations could possibly be attributed to an unsteady wake or to the existence of multiple steady positions. These possibilities cannot be directly investigated with a crossflow model for the wake development. However, a three dimensional model for the vortex wake configurations can be examined for multiple steady solutions.

1.2 Model Objectives

A three dimensional model is proposed which replaces the wake behind the missile or aircraft nose shaped body with line or curve vortex singularities and finds a steady configuration. This procedure makes no attempt to model the mechanism by which the vorticity moves into the vortices but rather is concerned with the positions of the separated vortices and the influence of those on the body. Typical vortex strengths and initial positions are taken from the experimental results and cross-flow calculations. The objectives of this study are to

- develop a three dimensional model for positioning vortex singularities in a steady configuration,
- evaluate the resulting vortex positions by comparison with experimental positions,
- examine the forces on the body as a result of the vortex wake and use those comparisons to improve the model,

- examine the possibility of multiple steady vortex positions for the same body and flow configuration,
- and to find the limitation of such a model by examining the detailed distributions of loads and pressures on the body.

CHAPTER 2. SOLUTION METHOD

The basis of the model stems from the inclusion of the influence of concentrated vortex filaments with the Neumann potential flow solution technique developed by Smith and Hess (21). The algorithm starts with an initial guess for the vortex positions, solves for the velocities induced by the vortices and then finds the contribution to the flow necessary to satisfy the zero normal flow boundary condition of the body. The vortices are then repositioned to align with the flowfield. The procedure is continued with the new positions until a convergence criterion is satisfied.

Three vortex models are examined, denoted the straight, segmented and curved vortex models.

2.1 Potential Solution

The flow is assumed to be inviscid, incompressible[†] and irrotational except for along the isolated vortex singularities. The flow velocity can be written as a superposition of the uniform free stream \bar{U}_∞ , the vortex induced contributions \bar{U}_v and a potential velocity $\nabla\phi$ which decays away far from the body. This velocity vector has the form

$$\bar{U} = \bar{U}_\infty + \bar{U}_v + \nabla\phi. \quad (2-1)$$

In the flowfield, the potential satisfies

$$\nabla^2\phi = 0. \quad (2-2)$$

Denoting the body surfaces as S , the Neumann boundary condition results from

$$\bar{U} \cdot \bar{n} = 0 \text{ on } S, \quad (2-3)$$

or,

$$\nabla\phi \cdot \bar{n} = -(\bar{U}_\infty + \bar{U}_v) \cdot \bar{n} \quad (2-4)$$

Following the procedure of Smith and Hess, the solution to (2-2) with the constraint that ϕ tends to zero far from the body and the boundary condition (2-4) can be expressed at any point \bar{p} in the flow as

[†]Compressibility effects can be approximated by the use of the Gothert transformation.

$$\phi(\bar{p}) = \iint_S \frac{\sigma(\bar{q})}{r(\bar{p}, \bar{q})} ds, \quad (2-5)$$

where \bar{q} lying in the surface is the integration variable and $r(\bar{p}, \bar{q})$ is the distance between the points. Substitution of (2-5) into the Neumann boundary condition for \bar{p} tending to the surface yields the equation for the source density σ ,

$$2\pi\sigma(\bar{p}) - \iint_S \sigma \frac{\partial}{\partial n} \left(\frac{1}{r(\bar{p}, \bar{q})} \right) dS = - (\bar{U}_\infty + \bar{U}_v) \cdot \bar{n}. \quad (2-6)$$

The solution of this integral equation can be approximated by considering the body as number of flat panels of constant σ .

The linear system resulting from the discretization of equation (2-6) is solved using the modified Gauss-Siedel described by Hess. After the first iteration of the position algorithm, the previous iteration's solution for the source density distribution σ can be used as an initial guess in solving the linear system.

For ease in notation a Cartesian coordinate system is assigned to the body with the origin at the nose tip, the x-axis extending along the body centerline and the y-axis in the angle of attack plane. All distances are scaled by the body length and velocities by the free stream velocity. Many of the experimenters use the base diameter to characterize the length scale in the publication of their results. The coordinates can be stretched to allow direct comparison with these results by taking the model distances times the fineness ratio f . Comparisons in the later section use this to plot equivalent values.

2.2 Straight Vortex Method

The simplest vortex singularities to include in the wake are the line vortices. As shown in Figure 2a, the wake is modelled by straight line vortices extending from the connection points on the body. The approximate images inside the body connect the vortex lines from the opposite sides of the body. The image vortices reduce the circumferential gradients in the source density, allowing a more sparse panelling. The images are approximated by a series of vortex segments connecting the crossflow image positions. The vortex induced velocity at any point not on one of the

vortices can be written as a sum of the components from each vortex and from the images. These components follow directly from the Biot-Savart law and are derived in the appendix. The vortex induced velocity at any point along one of the vortices is computed by summing the components from each of the other vortices and the images. There is no self-induced velocity for a straight line vortex.

The positioning algorithm attempts to align the vortex with the flow in a time-like fashion. A number of points along each line are convected with the flowfield using an Euler time step approximation. A line drawn through the new points in the best least squares sense is chosen as the new position for the vortex. The reference points are then redefined to lie on the newly positioned line vortex. A straight line cannot generally align closely with the flowfield both near and far from the body. The reference points can be positioned or weighted according to that region being modelled.

2.3 Segmented Vortex Model

To allow the vortex to align with the flow in a larger part of the wake region, the line can be kinked into connected segments (see Figure 2b). The design of this model is for two or three segments with a number of reference points marking out each segment. The approximate images and induced velocities away from the vortices are treated as in the straight vortex case.

By choosing the reference points to lie away from the segment endpoints, the calculation of the self-induced velocity can ignore the segment on which the point lies. The vortex induced velocity at each reference point results from summing over all the images and the vortex segments except the segment on which the point lies.

The positioning algorithm treats each segment similar to the line vortex model. The segments closest to the body are repositioned first, using the best fit line through the convected reference points. The length of the segments are to remain unchanged, so that once the initial segments are positioned, the initial point for the next segments are determined.

The direction of these segments is determined by the best line through the convected reference points associated with them. The last reference point in each segment can be associated with the next segment in the repositioning, since the vortex axial flow can convect the fluid element that the point represents into the region represented by that next segment.

In this model the segments must be long enough that the curvature effects associated with the bends are unimportant at the reference points. A more complex model results when the segment lengths are allowed to be sufficiently small that for computing the self-induced velocities the vortex is treated as a curve. This will be denoted as the curved vortex model.

2.4 Curved Vortex Model

The velocity induced at any point in the flow not lying directly on one of the vortices is determined as in the segmented vortex model with the exception being a slight change in the image calculation. The images are usually determined by connecting the crossflow images of the segment endpoints over ninety percent of the body. For bodies with noncircular cross section, the images are taken as straight segments from the attachment points of the vortices to a common connection point near the tail end of the body.

The velocity induced at a point lying on one of the segments is computed by modeling the closest region of the vortex by a circular arc through the nearest three segment endpoints and assuming a finite vortex structure. This self-induced velocity is discussed in detail in the appendix. The velocity induced by the other segments on the vortex are computed as before.

The positioning algorithm assigns a single reference point to each segment. The vortices are repositioned by aligning the segments with the velocity field calculated at the corresponding reference points. In this procedure the segment lengths are held constant and the initial segments (connecting to the body) can either be aligned with the surface streamlines or held with unchanged direction. This last option arises to give the freedom to choose some off-body points through which the vortices must pass.

CHAPTER 3. MODEL EVALUATION

In an attempt to limit the investigation and allow the model to be tested, the number of flow conditions and body shapes have been restricted to those corresponding to the most accessible experimental results. Most of the analysis was done for a tangent ogive cylinder with nose fineness ratio of 2.59 and total fineness ratio of 10.3. This corresponds to the MX configuration denoted as N1B1 and can be compared with the tangent ogive reported by Clark and Thompson and Morrison. Some other body shapes are examined in Section 4.3, comparing positioning results for ogive noses with elliptical cross section.

The experimental flow conditions are characterized by the Mach number, Reynolds number and angle of attack. Since the water tunnel experiments of Clark and Spangler and Mendenhall are used for estimating the initial positions and for positioning comparisons, the model is run at zero Mach number. The Reynolds number effects can enter the model only in the vortex attachment points and the core radius. The behavior of these parameters with variation in Reynolds number is not obvious and could provide a study in itself. The attachment points are taken from Clark's experiments when possible. Other sources will be credited when the appropriate case results are given. The core radius is taken as one tenth the body diameter. This seems to be of the appropriate scale and does not appear to cause drastic changes for small variations. The angle of attack range for applicability of the model needs to be determined. For small angle of attack the body pressure distributions indicates either no flow separation (or a negligible effect of flow separation) over most of the body. For slightly larger angles the flow separates, but the vortices formed do not separate from the shear layer before the end of the body. Results in this range of angle of attack cannot be consistent along the body because the vortices in the model must have constant vorticity. However, the pressure distribution at a particular axial station may agree with experiment as in Figure 3. The angles of attack of interest for applying the model are those large enough to exhibit non-zero side forces. Judging from the MX integrated pressures, the side force versus angle of attack curve appears to deflect from zero at 30° angle of attack (see

Figure 4). At the angle of 45° an asymmetric wake is the more common configuration. These two angles are chosen as the primary test angles. Other angles are used when the experimental values are not given at 30° or 45° and to examine variations with angle of attack.

Panel Parameters

The panels used to represent the body are formed by splitting the body into 30 bands along the body axis with two concentric bands on the tail end. Each band is then split into 24 panels by cuts through the x-axis. On the leeside of the body 15 of the 24 panels are positioned with even spacing. The concentration on this side is designed to allow better resolution in the region of rapid changes due to the vortex influence. Numerical experimenting indicates that the number of panels needed to examine the positioning algorithm is much smaller than the above, but the large number is necessary to resolve the body forces with this first order panel method.

For the cases examined in this study, the number of panels is the dominant factor in determining the cost for each iteration of the positioning algorithms. For the numbers described above, the computer time runs about 25 CPU seconds on a CDC 7600.

3.1 Potential Assumption

The assumption that the potential flow approximation is valid away from the wake region can be examined by looking at the pressures for low angles of attack and along the windward side of the body. In Figure 3 the circumferential coefficient of pressure distribution is plotted for increasing angles of attack along with typical wind tunnel measurements from the MX tests. These are taken at an axial station at about 35 percent along the body. The windward meridian of the body marks the origin for theta in this figure. As the angle of attack increases the values of the pressure coefficient on the leeside deviate from the potential solution without vortices. The presence of the vortices tends to correct the curve toward the experimental values for the case and station shown in this figure; however, in this particular case the correction is far too small or too

large at other stations along the body. The pressure coefficients on the windward side of the body remain in good agreement with the experimental values even for larger angles of attack.

3.2 Vortex Parameters

The velocities induced in the model are defined by several parameters which must be determined from experiment. The number of vortices, attachment points, vortex strength and the singularity cutoff are all determined by comparison with experiments. The magnitude of vortex strength used is based on the correlation with angle of attack by Yanta and Wardlaw (20) for a similar body and has the form

$$|\Gamma| = .24 \sin \alpha, \quad (3-1)$$

where the vortex strength Γ is scaled by the body length and the free-stream velocity. The vortex attached closest to the front of the body is given vortex strength from 10 to 50 percent less than the value determined by (3-1). The strengths of the first and last vortices are adjusted to force the sum of the strengths from all the vortices to be zero. The value of $|\Gamma|$ given by (3-1) applies to the maximum strength.

The number of vortices and attachment positions included in the wake also depends on the angle of attack. Clark (13) correlated the extrapolated vortex attachment position for up to about four vortices over a wide range in angle of attack. These attachment positions are used in the model for vortices attaching before about 90 percent of the body length. The point around the body to which the vortex attaches seems to have little effect on the final vortex position when the curved vortex model is used. An input error resulting in all the vortices attaching on the same side of the body did not result in significantly different converged positions.

The singularity cutoff is determined by testing the model over a range of values and judging the resulting forces and vortex position against the experimental values to fix a single value for further use of the model. The analysis of this parameter is discussed further in Section 3.4.

Care must be taken in judging flow visualization to give input to the model. A picture taken during the MX wind tunnel experiment is shown as Figure 5. The wake appears to contain a pair of asymmetric vortices extending from the body. Measuring the position from the top and side view pictures and using these as initial positions, the straight line model gave the converged positions indicated by the views from the side and above as shown in Figures 6 and 7. Although the side view is similar to the experimental picture, the view from above is not. The experimental view from above the model shows the vortices lying directly above the cylinder, while in Figure 7 they move off to the left. This can be corrected by adding a third vortex, unseen in the experiment. The inclusion of a weak third vortex pulls the original pair back above the body as shown in Figures 8 and 9.

3.3 Positioning Algorithm

The number of iterations required for convergence varies considerably between the three models. The curved vortex model converges rapidly for a small number of segments. In those cases with less than forty vortex segments (excluding images) convergence occurs in about ten iterations. For much larger numbers of segments the required number of iterations increases significantly unless a good initial guess for the vortex positions is available.

The straight line model uses an approximation to the time dependent behavior to relax to the steady solution. Forty iterations of the positioning algorithm would not be uncommon for the model with two vortices. Some test cases do not converge to a steady solution, but have an oscillatory behavior. These are examined further in Section 4.1.

The segmented vortex model has the worst positioning behavior of the three models. The number of iterations required for convergence appears prohibitive. Unlike the straight line model which is somewhat predictable at each iteration step based on the previous few steps, the segmented model can make large changes in position. The constraint that the segments remain of constant length appears to cause erratic behavior in the segments away from the body. The same oscillatory behavior seen in the line vortex

model may also be appearing in the first segment of the segmented model. No further studies have been conducted for this model. The positioning algorithm must be modified before it can be used.

3.4 Singularity Cutoff

The cutoff distance in the vortex induced velocity only becomes important in that region where the vortex attaches to the body. Any panel control points close to the vortex or vortex reference point close to its image can feel an induced velocity of unrealistic magnitude. The effect of the cutoff parameter is to smooth out those induced velocities, acting to at best crudely imitate the shear layer in this region. At larger angles of attack, when the vortices are attached to the body through the shear layer for only a small distance, the effect of this crude approximation is felt over a small portion of the body.

The effect of variations of the cutoff parameter on the vortex positions can be used to eliminate ranges of values for that parameter. The relation of the cutoff to the segment length in the curved vortex model or the reference point separation in the straight vortex model greatly effects the positioning. When the cutoff and segment length are both small in the curved vortex model, the calculations of the first or second vortex segment directions are dominated by the image induced velocity. A vortex with segment lengths sufficiently large to prevent the first few segments from lying too close to the body surface can develop sharp bends for low angles of attack if a later segment moves near to the body. For 30° angle of attack and vortices attached symmetrically at $x = .125$ the vortices stay close to the surface for about fifty percent of the body length. The converged positions varied considerably with the choice of the cutoff parameter. At larger angles of attack the vortices move away from the body quickly, reducing the effect of the cutoff except on the first segment position. If the cutoff parameter is too large, the curved positioning algorithm can align the vortices with the vortex free potential flowfield. These considerations, along with a constraint on the total number of segments, give bounds on the value of the cutoff parameter and the segment lengths for the curved vortex model. The nominal values used for the segment lengths are .05 for the initial segment and .1 for all remaining

segments on a vortex. The vortices extend to about twenty percent beyond the body above the x-axis, then align with either the free stream or the asymptotic slope.

In the straight vortex model the reference points nearest the bodies are lightly weighted in the positioning algorithm to alleviate the sensitivity to the cutoff parameter. However, the effect of increasing the cutoff at smaller angles of attack (30° or less) is to move the symmetric vortices closer together. This behavior makes the cutoff value difficult to access, though extreme values can be eliminated.

Once the range for the cutoff parameter has been determined for the 30° angle of attack, the final test values are taken as the minimum values in that range. These values are .01 for the curved vortex model and .02 for the straight vortex model. The values large enough to prevent positioning problems for the 30° angles of attack are easily large enough for the 45° cases. A test case for the curved vortex model at 45° angle of attack to verify the choice of parameters discussed above converges in ten iterations and compares well with experimental force coefficients. The model normal and side force coefficients have magnitudes of 5.1 and 1.3. The corresponding values from the MX tests at .4 Mach number range from 4.0 to 5.6 and 0.1 to 1.9 for various Reynolds numbers. The side view of the final positions appears as Figure 13.

CHAPTER 4. VORTEX POSITIONS

Two aspects of the positioning algorithm behavior are of interest. The computed vortex positions can be compared with the results of flow visualization experiments. Also, the non-uniqueness of the steady solutions steady solutions can be examined.

4.1 Straight Vortex Positions

At 30° angle of attack the straight line vortex model with two vortices constrained to be symmetric does not converge in the first twenty iterations. A plot of the crossflow positions of the vortices shows the behavior to be oscillatory. The positions of one of the vortices for two initial conditions is shown in Figure 10. The conjecture for this case is for the existence of a (neutrally) stable point lying inside the inner loop in Figure 10. If the initial condition were for a vortex passing through this point, perhaps the algorithm would not move the vortex.

The 45° angle of attack results for the straight line model have been discussed in Section 3.1 and shown in Figures 8 and 9 as an example of the effect of additional vortices on the positions. The direction of the asymptotes for the straight vortex model can be compared with those measured by Clark in the water tunnel or Thompson and Morrison at low Mach number. If the vortices make an angle ξ with the body axis in the angle of attack plane, then the parameter

$$\chi = \tan \xi / \tan \alpha \quad (4-1)$$

is used to correlate the data. For the straight vortex results at 45° the value of χ is .53, smaller than the typical experimental value of 0.8. However, since the straight model does not locally align with the flow, but rather aligns with the average velocity, the direction cannot be expected to agree with the asymptotic direction.

4.2 Curved Vortex Positions

To demonstrate a lack of uniqueness for the vortex positions when the initial positions are varied requires only a single counterexample. However, a number of test cases were run without any distinct multiple

solutions. Symmetry in the initial condition yielded symmetric positions except when the vortex strengths were taken to be asymmetric. The positions then lost the symmetry. When the strength of the vortices were set back to be symmetric and the asymmetric positions used as initial conditions, the vortices returned to the symmetric configuration identical to that for the symmetric pair with symmetric initial conditions.

To compare the vortex curve positions with the experiments of Clark and Thompson and Morrison, a series of cases were run for angles of attack of 35° , 40° , 45° , 50° , and 55° following the guidelines for choosing the parameters. The 45° cases were run for both three and four vortices. The resulting vortex positions are shown in Figures 11 through 16. The values of χ given by Equation (4-1) are plotted in Figure 17 for the angles measured from the position pictures, the asymptotic angles and the range of possible measured angles. Included as well are the value from Clark's experiments and the estimated values from the lowest Mach number results of Thompson and Morrison. All of the experimental values fall in the range of the possible measurements from the model.

For the 30° angle of attack symmetric cases the vortices stay much closer to the surface than is observed or predicted by the crossflow calculations. One possible explanation for this behavior is the absence of a shear layer in the model. The resulting constant strength vortex pair mutually induce velocities holding them close to the surface. The cutoff large enough to prevent what could be interpreted as erratic behavior nullifies the image effect.

4.3 Elliptic Nose

The experimental study of Spangler and Mendenhall includes an ogive nose of elliptical cross section for both major axis horizontal and major axis vertical with respect to the freestream. The fineness ratio based on the equivalent base diameter is 5.0 and the ratio of the major to minor axis in the cross section is 1.44. The experiments were run in a water tunnel using flow visualization to indicate the position of the first two vortices. An estimate for the vortex strengths was also determined from flow measurements. These parameters can be inserted directly into the

curved vortex model to examine the positioning algorithm. The vortices not indicated in the experiment must be given an estimated position and the vortex which lies very close to the body approximated by a single fixed segment. The resulting positions for the first two vortices are shown in Figures 18 through 21, with the experimental values indicated by the dashed lines. For the major axis vertical case the first vortex lies slightly above and outboard from the experiment. In Figure 20 the side view of the major axis horizontal positions do not agree as well. The attachment point may be too far forward in this case and the shear layer continues to feed the vortex beyond the estimated position. The view from above shown in Figure 21 shows the nose vortex lies directly above the experimental position.

CHAPTER 5. BODY FORCES AND LOAD DISTRIBUTIONS

In the evaluation of the choice of the cutoff parameter the agreement of the test case force coefficients with the MX wind tunnel experiments was mentioned. These need to be examined in more detail in order to evaluate the model.

5.1 Variations of C_N and C_Y with α

The cases run for Section 4.2 to examine the behavior of the vortex positions with angle of attack also gave force coefficients. The values of the normal force coefficient C_N is plotted against angle of attack in Figure 22. The solid symbols indicate the model approximation to the value for C_N . Two of the values listed on this figure will be discussed in Section 5.2. The empty symbols are from the MX wind tunnel experiments at the lowest Mach number and a variety of Reynolds number.

The equivalent values for the side force coefficient are much greater than the experimental coefficients for most angles of attack. A more careful examination of the forces can turn up the reason for the inconsistency between the agreements of the normal and side force coefficients.

5.2 Cutoff Sensitivity

Another form in which to examine the body forces is through the load distribution. The normal load distribution c_n is the local contribution to the normal force coefficient based on the body diameter. To be consistent with the MX wind tunnel test, the results from the curved vortex model with three vortices are converted to dimensions based on the body diameter. The resulting distributions are plotted in Figure 23 for several values of the cutoff parameter. The effect of the vortices appear to be centered in the region immediately trailing the vortex attachment points. The wake prevents the potential fall off after the rise on the nose, but once the vortices move away from the body, the curve falls through zero. As a result the last twenty percent of the body gives a misleading contribution to the normal force coefficient. If these end effects were eliminated by including more (but weak) vortices, the effect should be to

increase the C_N as shown in Figure 22. The values of C_N adjusted by neglecting the normal load where the curve falls to zero are indicated by the solid squares and the values of C_N which interpolate the normal load from ahead of the drop off in c_n are indicated as corrected for end effects by the solid diamonds. Both of these values are much higher than the experimental values, but larger C_N would have resulted in the value of the cutoff parameter recognized as too small. For increasing values of the cutoff the behavior of the load distribution become more reasonable.

5.3 Side Load Distribution

The over-estimates in the side force coefficient discussed in Section 5.1 are consistent with the results of the last section. The side load distribution plotted in Figure 24 for several values of the cutoff parameter indicates an order of magnitude over-estimate when compared to the experimental side force distribution. A possible reason for these peaks is that the asymmetric vortices are not balanced by opposing shear layers at the point of detachment. All the vorticity is concentrated near one side of the body at the first attachment points; then at the second stronger vortex the effect is switched. For the three vortex model with a cutoff of .01, the opposing components of the side force due to the two large peaks cancelled a large contribution, resulting in an estimate which agreed with experiment.

CHAPTER 6. DISCUSSIONS AND CONCLUSIONS

A method has been developed to predict the three dimensional vortex flow field of aerodynamic bodies at high angle of attack. The panel method developed by Smith and Hess is modified to solve the Neumann potential flow problem with the addition of vortex filaments which approximate the wake. Three models for the vortex wake were examined. Straight line, segmented, and curved filament models were tested at several angles of attack on ogive cylinder and elliptical cross section bodies.

Results of the present study showed that the curved vortex model could predict the positions of the vortices in the wake with good accuracy for angles of attack greater than 30 degrees. However, the empirical input required to obtain these results limits the models usefulness as a design tool. Currently the vortex strengths and attachment points must be approximated for use in the model.

One way to reduce the empirical input and to improve the method would be to model the effects of the feeding shear layer. The shear layers could be approximated using panels with a double layer or dipole density to represent the vortex sheet. Similar methods have been developed to model the roll up behind a delta wing.

The predicted normal and side forces are sensitive to the singularity cutoff. The purpose of the cutoff is to eliminate the singularity for numerical reasons and smooth the induced velocity in the panels nearest the vortex. Adjusting the cutoff range in a consistent fashion to eliminate the sharp peaks, but not to eliminate the augmented loads, should be possible. However, the panel size, vortex segment length and angle of attack need to be considered when fixing the cutoff value. Since the method uses a single reference point in each panel at which to enforce the Neumann boundary condition, the vortex induced velocity on the entire panel is judged by the value at the reference point. A large induced tangential velocity at the panel point creates a pressure peak which is attributed to the entire panel in the force calculation. Controlling these peaks with the cutoff parameter and adjusting the vortex attachment points to a maximum distance from the panel reference points tend to smooth the load distribution, but the physical mechanisms of the wake near the body are not

being modelled. The large over-estimate in the side force distribution and the failure of the model at lower angles of attack demonstrate the need for a higher level of sophistication in the model near the body before reasonable forces can be extracted.

One of the primary objectives of the present work was to examine the possibility of multiple stable vortex positions. In no case did the curved filament model show the existence of multiple solutions for the same vortex conditions. The oscillatory behavior of the straight line model at 30° angle of attack probably arises due to the balance of the effects on the vortex near the body with the effects away from the body under the constraint that the vortex remains straight and cannot be used to conclude that large scale unsteady vortex configurations are responsible for variations in the side force measurements.

The inability of the curved model to predict multiple positions indicates that experimentally observed multiple positions arise because either the vortex attachment points are changing or the vortex strengths are changing. Both of these may result from unsteady or quasi-steady boundary layer separation.

APPENDIX -- VORTEX INDUCED VELOCITIES

The velocity induced by a vortex line or curve can be evaluated from the Biot-Savart integral,

$$\bar{U}_v(\bar{p}) = -\frac{\Gamma}{4\pi} \oint \frac{(\bar{p}-\bar{q}) \times d\bar{q}}{|\bar{p}-\bar{q}|^3}, \quad (A-1)$$

where \bar{q} lies along the vortex, \bar{p} is some point off the vortex and $d\bar{q}$ denotes the directed element.

For vortices approximated by a set of straight segments, the contribution to the integral of each straight section can be evaluated in closed form. The induced velocity due to a segment extending from \bar{q}_0 to \bar{q}_1 can be written

$$\bar{U}_v^i(\bar{p}) = \frac{\Gamma}{4\pi} \frac{\bar{s} \times (\bar{p}-\bar{q}_0)}{|\bar{p}-\bar{q}_0|^2 - (\bar{s} \cdot (\bar{p}-\bar{q}_0))^2} \left(\frac{\bar{s} \cdot (\bar{q}_1-\bar{p})}{|\bar{q}_1-\bar{p}|} + \frac{\bar{s} \cdot (\bar{p}-\bar{q}_0)}{|\bar{p}-\bar{q}_0|} \right), \quad (A-2)$$

where

$$\bar{s} = (\bar{q}_1-\bar{q}_0)/|\bar{q}_1-\bar{q}_0|$$

is the normalized direction of the vorticity vector, and the superscript (i) denotes the i^{th} segment. The contribution due to a semi-infinite ray can be obtained by taking the limit as \bar{q}_1 tends to infinity, giving

$$\bar{U}_v^i(\bar{p}) = \frac{\Gamma}{4\pi} \frac{\bar{s} \times (\bar{p}-\bar{q}_0)}{|\bar{p}-\bar{q}_0|^2 - (\bar{s} \cdot (\bar{p}-\bar{q}_0))^2} \left(1 + \frac{\bar{s} \cdot (\bar{p}-\bar{q}_0)}{|\bar{p}-\bar{q}_0|^2} \right) \quad (A-4)$$

As the point \bar{p} approaching a vortex segment, the induced velocity increases like the reciprocal of the distance. In order to prevent the unrealistic singularity from affecting the solution, a separate form for $U_v^i(\bar{p})$ is used when the distance

$$R(\bar{p}) = \left(|\bar{p}-\bar{q}_0|^2 - (\bar{s} \cdot (\bar{p}-\bar{q}_0))^2 \right)^{\frac{1}{2}} \quad (A-5)$$

from the point \bar{p} to the segment is less than some specified cutoff distance c_0 . The velocity

$$\bar{U}_v^i(\bar{p}) = \frac{\Gamma}{4\pi} \frac{\bar{s} \times (\bar{p} - \bar{q}_0)}{c_0^2} R(\bar{p}) \left(\frac{\bar{s} \cdot (\bar{q}_1 - \bar{p})}{|\bar{q}_1 - \bar{p}|} + \frac{\bar{s} \cdot (\bar{p} - \bar{q}_0)}{|\bar{p} - \bar{q}_0|} \right) \quad (A-6)$$

decreases to zero with $R(\bar{p})$.

Self-Induced Velocity

When the Biot-Savart law is used to compute the induced velocity of a curved vortex on itself, the integral does not give a finite velocity. In order to subtract out the singularity without neglecting the self-induced velocity altogether, the segments approximation is refined and a vortex core structure is assumed. Moore and Saffman (21) and Widnall, Bliss and Zelay (22) demonstrated that the self-induced velocity of a curved vortex with specified vorticity distribution and core radius much smaller than its radius of curvature could be accurately approximated using the Biot-Savart law, but deleting a specified integration distance centered about the singularity. The integral cutoff distance ϵ has the form

$$\log \epsilon = \log (r_c/2) + \frac{1}{2} - \frac{4\pi^2}{\Gamma^2} \int_0^{r_c} r v^2 dr + \frac{8\pi^2}{\Gamma^2} \int_0^{r_c} r w^2 dr \quad (A-7)$$

where r_c is the radius of the vortex, Γ is the circulation and v and w are the local swirl and axial velocities associated with the vortex. The vortex structure depends on the Reynolds number and the shear layer vorticity distribution. Leonard (23) gives a form for the local contribution for a vortex ring with uniform vorticity in the core by constructing a circular arc through three of the reference points marking the vortex ring. This can be applied directly to the computation of the self-induced velocity on one of the segments of the curved vortex model by constructing a circular arc through the previous segment initial point and

the initial point and endpoint of the current segment as shown in Figure 25. Denoting the length of the two segments as ℓ_1 and ℓ_2 and the angle between the segments as θ , the radius R_c of the circular arc connecting the endpoints is given by

$$R_c = \left(\frac{\ell_1^2 + \ell_2^2 - 2\ell_1\ell_2 \cos\theta}{4\sin^2\theta} \right)^{\frac{1}{2}} \quad (\text{A-8})$$

The self-induced velocity due to the closest segments then reduces to

$$U_v^i = \frac{\Gamma}{4\pi R_c} \left(\log \left(\frac{8R_c}{r_c} \right) - .558 + \frac{1}{2} \log \frac{\ell_1\ell_2}{(2R_c + \sqrt{4R_c^2 - \ell_1^2}) (2R_c + \sqrt{4R_c^2 - \ell_2^2})} \right) \quad (\text{A-9})$$

where r_c is the core radius.[†] The contribution due the remaining sections of the vortex are computed using the segment formula.

[†]Notice that in Equation A-9 the axial velocity in the vortex has been neglected. This results from the assumption that the average axial velocity is small compared with the induced swirl velocity at the edge of the vortex.

REFERENCES

1. Thompson, K.S., and Morrison, D.F., "The Spacing Position and Strength of Vortices in the Wake of Slender Cylindrical Bodies at Large Incidence," *Journal of Fluid Mechanics*, Volume 50, Pt. 4, December 1971, pp. 751-783.
2. Fidler, J.E., and Bateman, M.C., "Asymmetric Vortex Effects on Missile Configurations," *AIAA Paper No. 75-209*, January 1975.
3. Kubin, J.S., "An Analysis of Steady Asymmetric Vortex Shedding from a Missile at High Angles of Attack," *Masters Thesis, Air Force Institute of Technology*, November 1973.
4. Kao, H.C., "Side Forces on Unyawed Slender Inclined Aerodynamic Bodies," *J. Aircraft*, Volume 12, No. 3, March 1975, pp. 142-150.
5. Bryson, A.E., "Symmetric Vortex Separation on Circular Cylinders and Cones," *Journal of Applied Mechanics*, Volume 26, December 1959, pp. 643-648.
6. Schindel, L., "Effects of Vortex Separation on Lift Distribution of Elliptic Cross Section," *Journal of Aircraft*, Volume 6, No. 6, November-December 1969, pp. 537-543.
7. Wardlaw, A.B., "Prediction of Normal Force, Pitching Moment, and Yawing Force on Bodies of Revolution at Angles of Attack up to 50 Degrees using a Concentrated Vortex Flow-Field Model," *NOL TR 73-209*, October 1973.
8. Angelucci, S.B., "A Multivortex Method for Axisymmetric Bodies at Angle of Attack," *Journal of Aircraft*, Volume 8, No. 12, December 1971, pp. 959-966.
9. Marshall, F.J., and Deffenbaugh, F.D., "Separated Flow Over Bodies of Revolution Using an Unsteady Discrete-Vorticity Cross Wake. Part 1 - Theory and Applications," *CR-2414*, June 1974.
10. Wardlaw, A.B., "Multivortex Model of Asymmetric Shedding on Slender Bodies at High Angles of Attack," *AIAA Paper No. 75-123*, January 1975.
11. Deffenbaugh, F.D., and Koerner, W.G., "Asymmetric Wake Development and Associated Side Force on Missiles at High Angles of Attack," *Journal of Spacecraft and Rockets*, Volume 14, No. 3, March 1977.

REFERENCES (CONTINUED)

12. Jorgensen, L.H., "Prediction of Static Aerodynamic Characteristics for Slender Bodies Alone and with Lifting Surfaces to Very High Angles of Attack," NASA TR R-474, September 1977.
13. Clark, W.H., "Body Vortex Formation on Missiles in Incompressible Flows," AIAA Paper No. 77-1154, August 1977.
14. Spangler, S.B. and Mendenhall, M.R., "Further Studies of Aerodynamic Loads at Spin Entry," ONR CR 212-225-3, June 1977.
15. Baker, D.C. and Reichenau, D.E., "Aerodynamic Characteristics of an MX Missile at Free-Stream Mach Number from 0.3 to 1.3 and Angles of Attack up to 180 Deg," AEDC-TR-75-34, April 1975.
16. Baker, D.C., "MX Missile Pressure Data at Free-Stream Mach Numbers from 0.3 to 1.3 and Angles of Attack from 5 to 55 Deg," AEDC-DR-99, September 1975.
17. Burchfield, C.G., "Asymmetric Vortex - Induced Side Force on an MX Missile at Roll Angles from -10 to 190 Deg at Free-Stream Mach Numbers from .4 to 1.5," AEDC-TR-76-169, December 1976.
18. Flaherty, J.I., "Experimental and Analytical Investigations of High Angle of Attack Missile Aerodynamics," AIAA Paper No. 77-1156, August 1977.
19. Owen, F.K. and Johnson, D.A., "Wake Vortex Measurements of Bodies at High Angle of Attack," AIAA Paper No. 78-23, January 1978.
20. Wardlaw, A.B. and Yanta, W.J., "Laser Doppler Velocimeter Measurements of Leeward Flowfields on Slender Bodies at Large Angles-of-Attack," AIAA Paper No. 77-660, June 1977.
21. Hess, J.L. and Smith, A.M.O., "Calculation of Nonlifting Potential Flow about Arbitrary Three-Dimensional Bodies," *Journal of Ship Research* Volume 8, September 1964.
22. Moore, D.W. and Saffman, P.G., "The Motion of a Vortex Filament with Axial Flow," *Philos. Trans. Roy Soc Lon.*, Volume 272, July 1972.
23. Widnall, S., Bliss, D. and Zalay, A., "Theoretical and Experimental Study of the Stability of a Vortex Pair," Aircraft Wake Turbulence and its Detection, New York; Plenum Press, 1971.
24. Leonard, A., "Numerical Simulation of Interacting, Three-Dimensional Vortex Filaments," Lecture Notes in Physics, Volume 35, Springer-Verlag, Berlin, 1975.

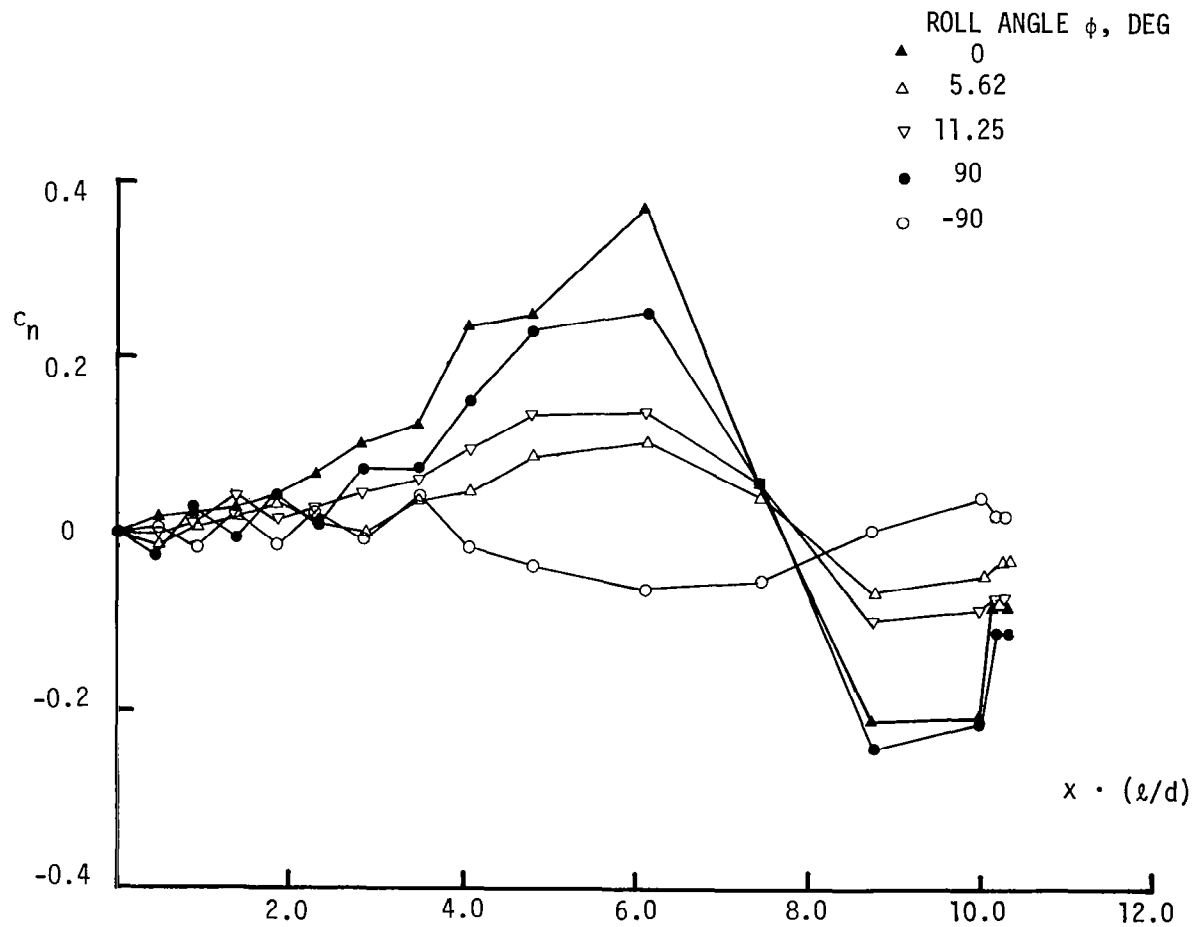


FIGURE 1. EFFECT OF ROLL ANGLE ON SECTIONAL SIDE FORCE COEFFICIENT DISTRIBUTION ON N2B1 AT 40 DEG ANGLE OF ATTACK ($M = 0.6$, $Rd = 3.17 \times 10^6$)

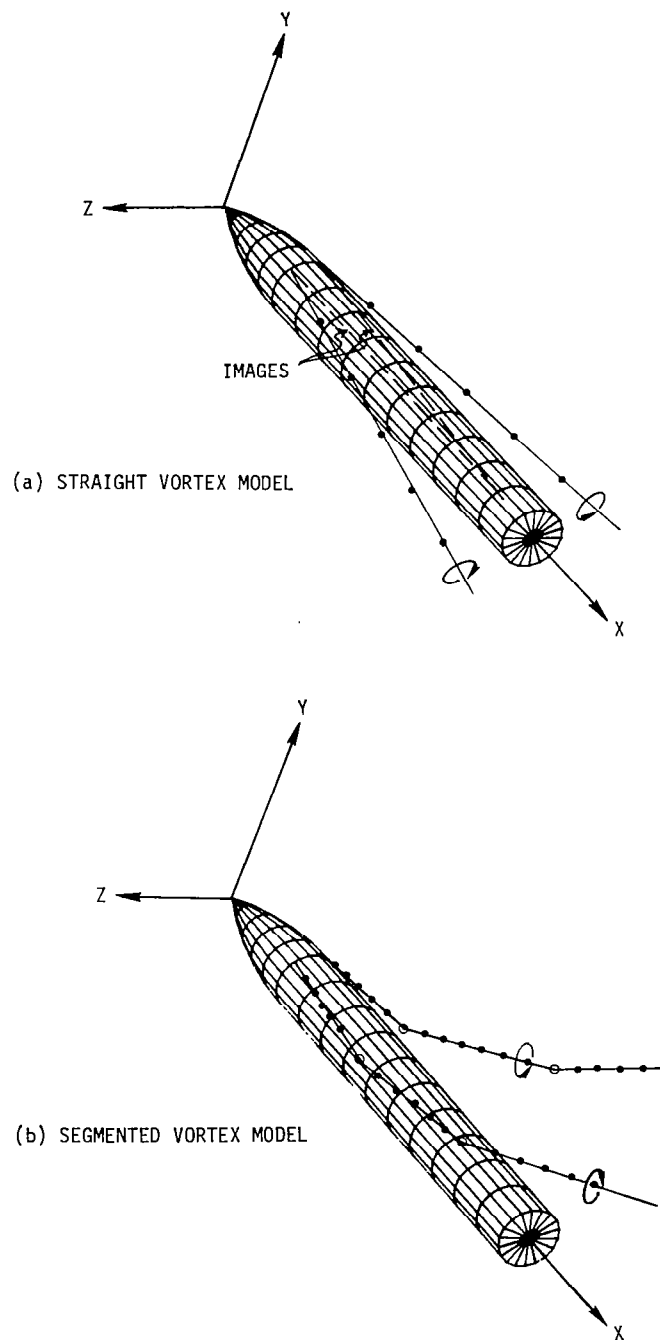


FIGURE 2. MODEL GEOMETRY SHOWING IMAGES AND VORTEX REFERENCE POINTS

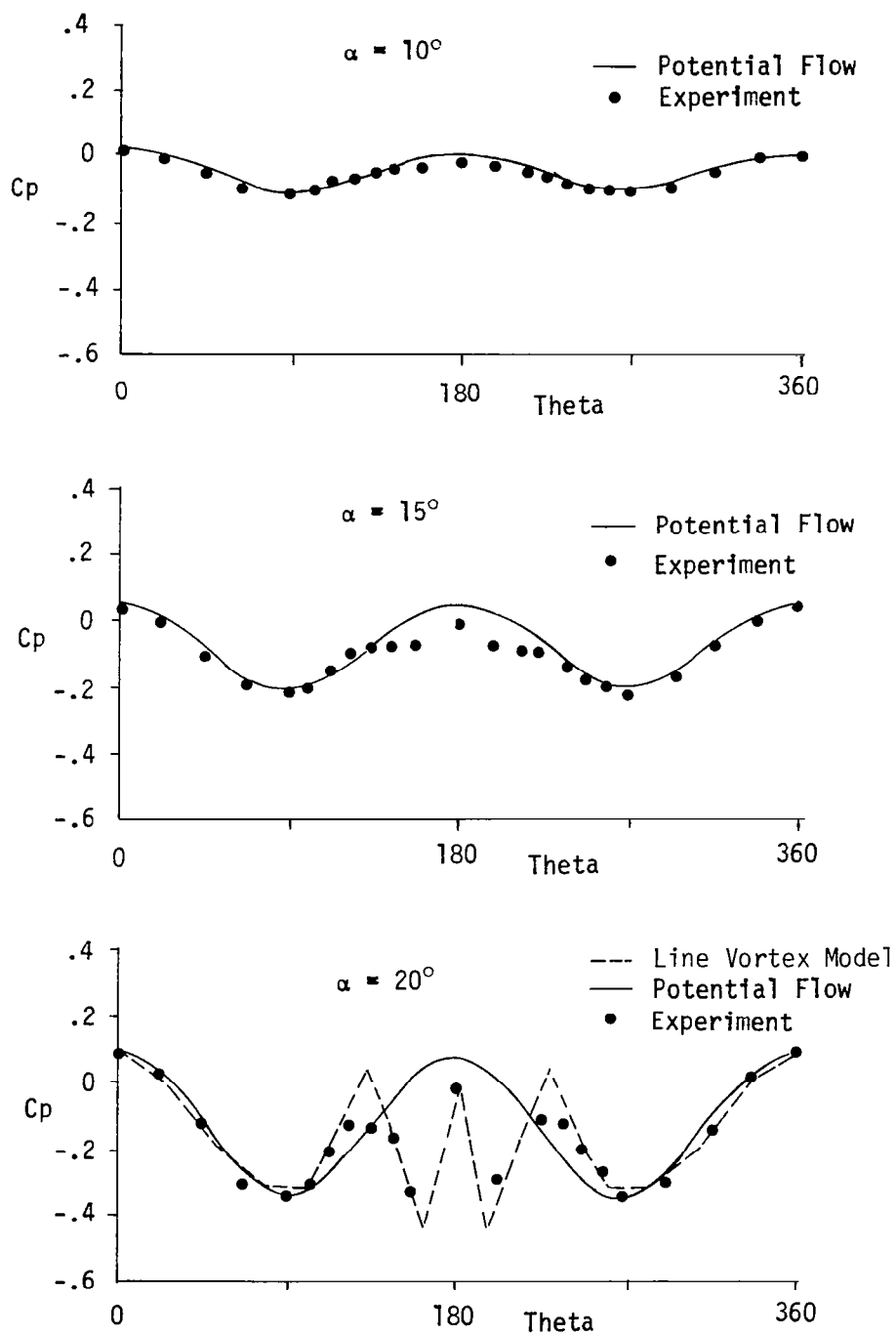


FIGURE 3. Potential pressure calculations compared with MX pressure measurements at axial station 35% down an ogive cylinder (N1B1). Line vortex model pressures included with $\alpha = 20^\circ$ potential pressures.

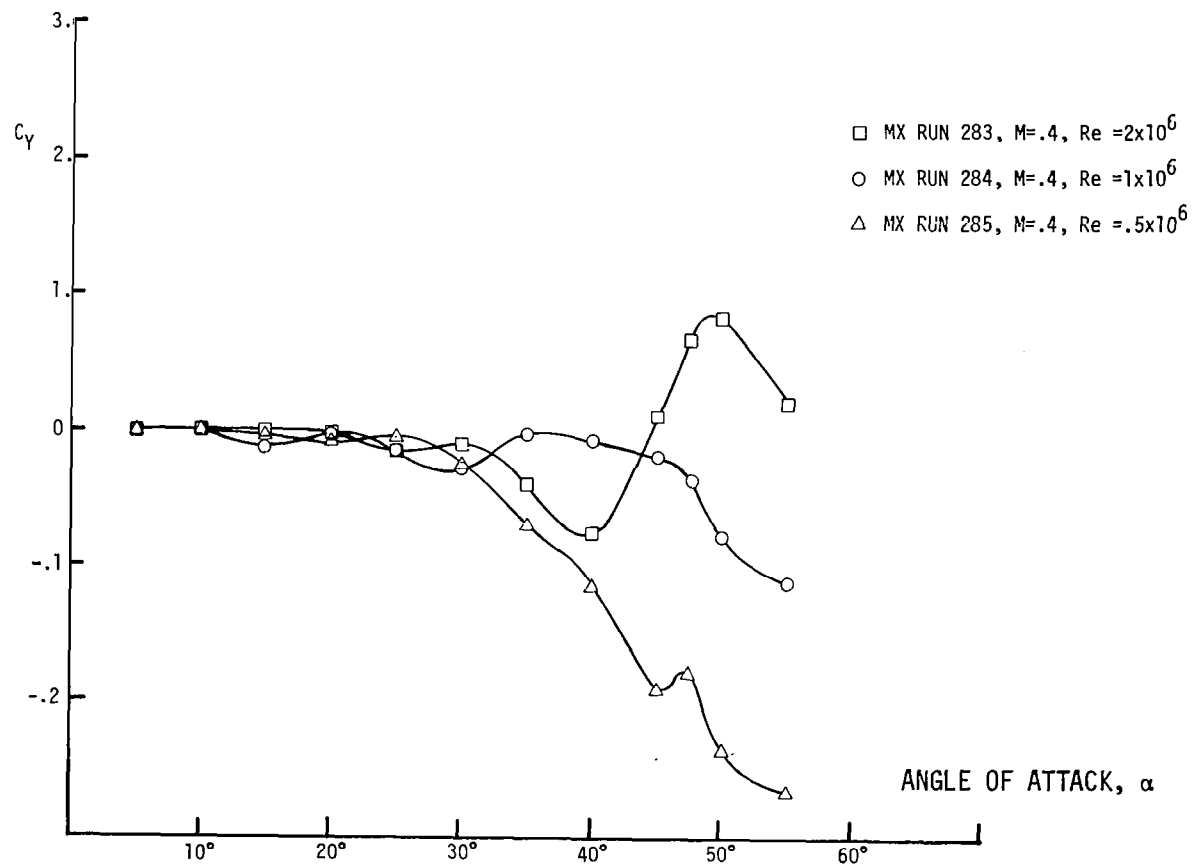


FIGURE 4. SIDE FORCE FROM INTEGRATING PRESSURES TAKEN
AT .4 MACH NUMBER IN THE MX WIND TUNNEL TESTS

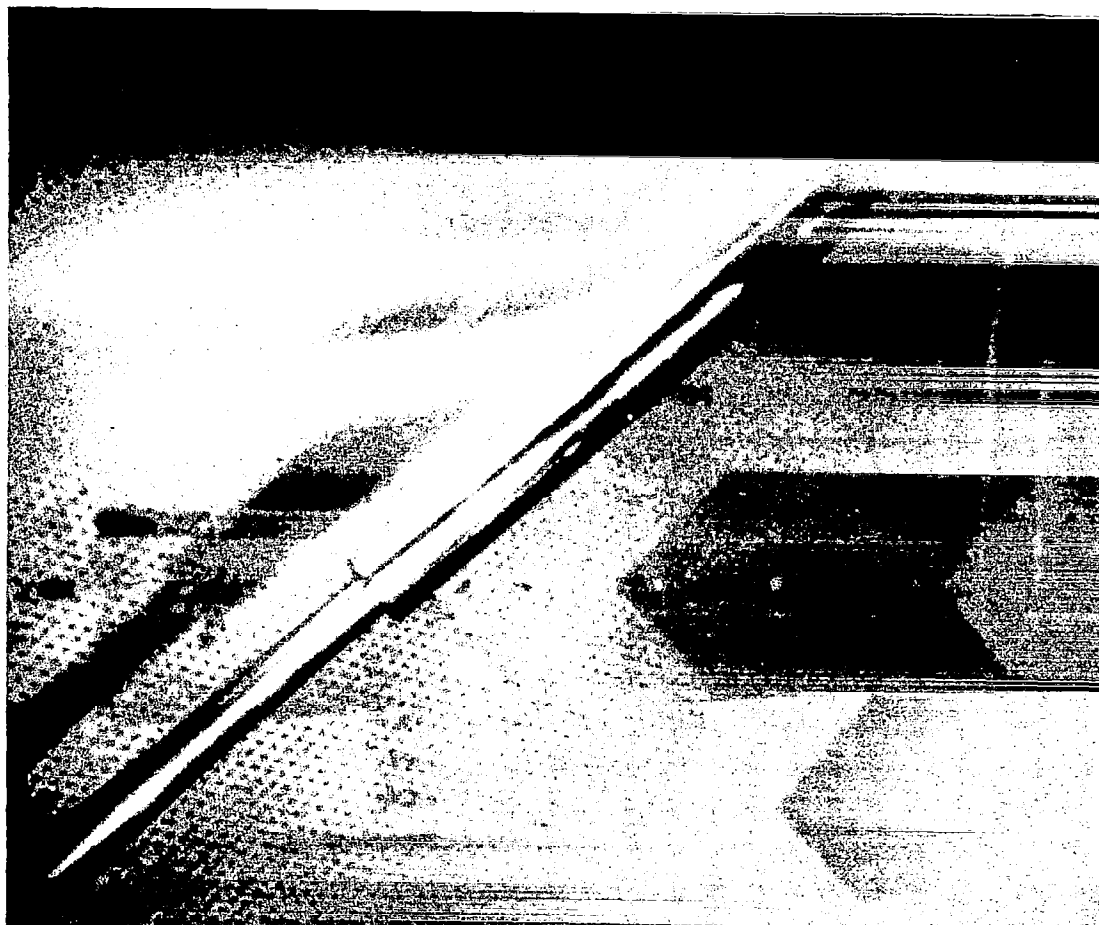


FIGURE 5. MX WIND TUNNEL TESTS

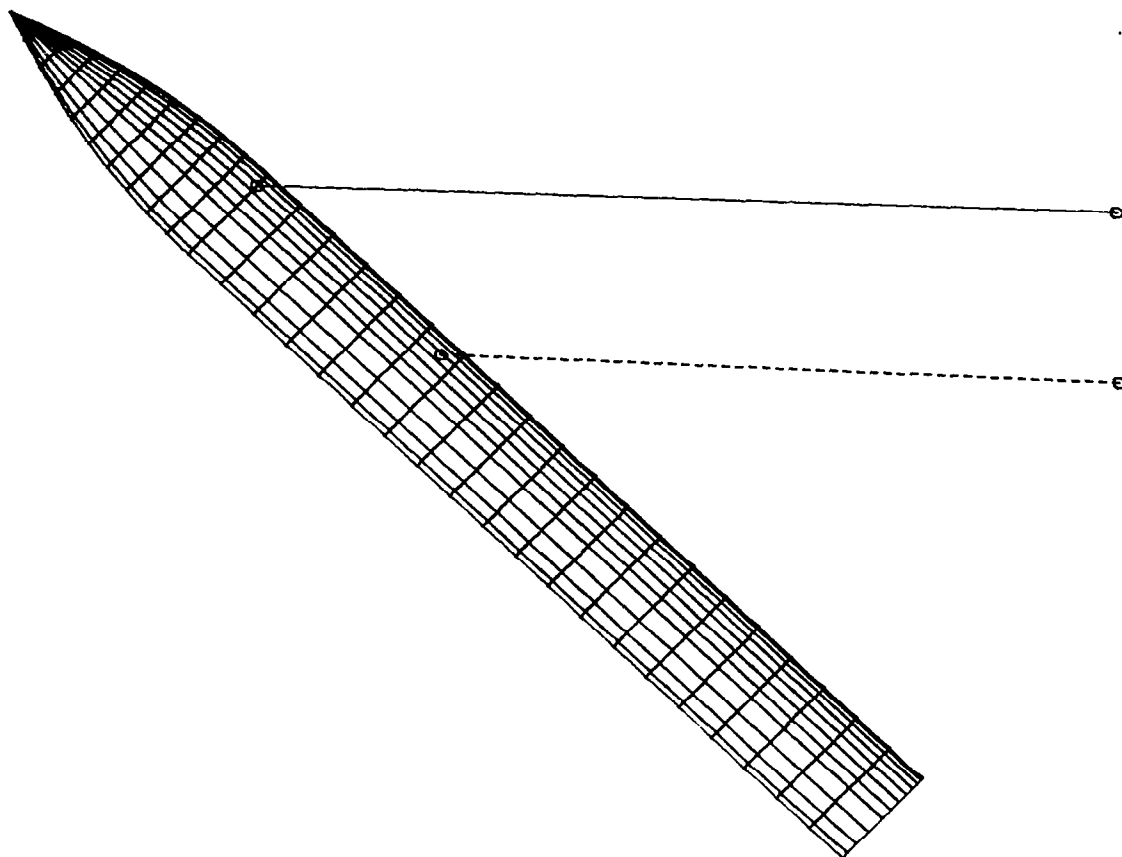


FIGURE 6. STRAIGHT VORTEX MODEL APPLIED WITH 2 VORTICES
FOR 45° ANGLE OF ATTACK, VIEWED FROM THE SIDE

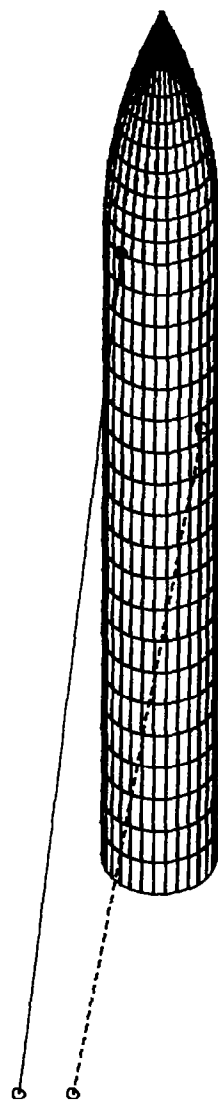


FIGURE 7. STRAIGHT VORTEX MODEL APPLIED WITH 2 VORTICES FOR 45° ANGLE OF ATTACK, VIEWED FROM ABOVE

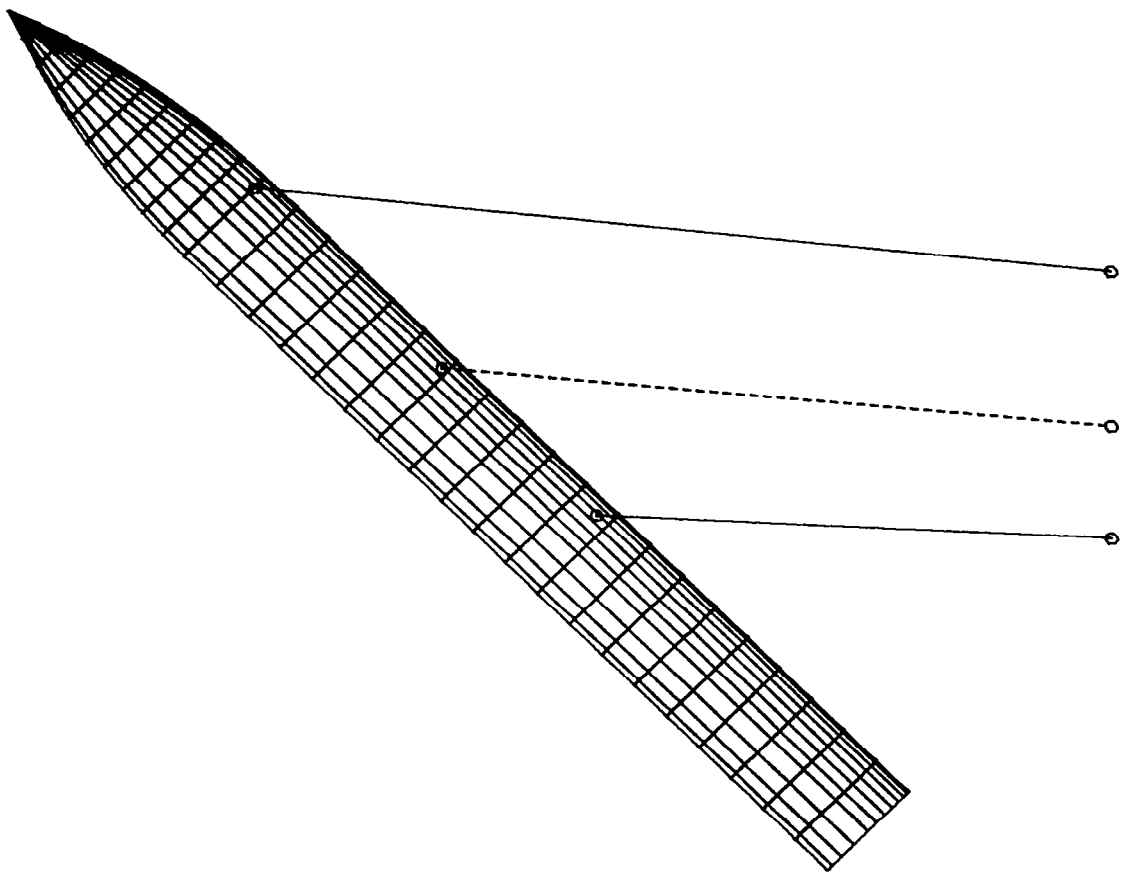


FIGURE 8. STRAIGHT VORTEX MODEL APPLIED WITH 3 VORTICES
FOR 45° ANGLE OF ATTACK, VIEWED FROM THE SIDE

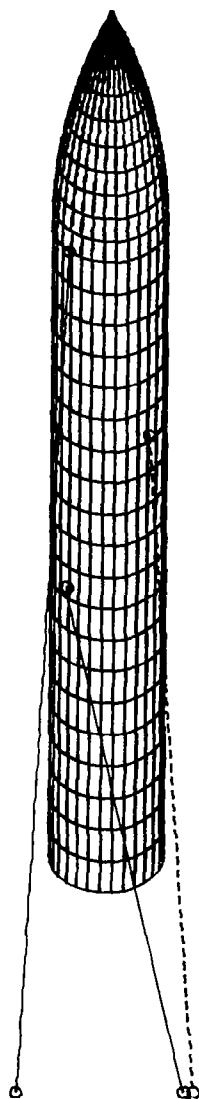


FIGURE 9. STRAIGHT VORTEX MODEL APPLIED WITH 3 VORTICES FOR 45° ANGLE OF ATTACK, VIEWED FROM ABOVE.

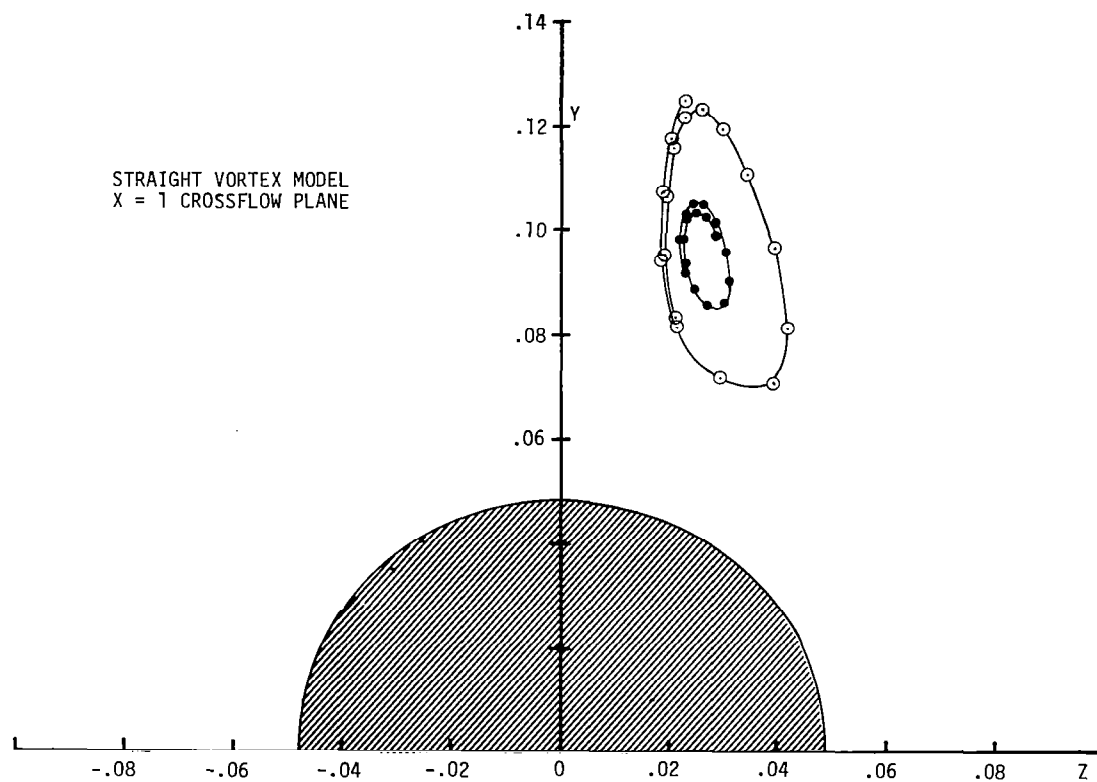


FIGURE 10. "OSCILLATING" SOLUTION FOR THE STRAIGHT LINE MODEL AT 30° ANGLE OF ATTACK. THE POSITIONS ARE MIRRORED BY THE SECOND VORTEX ACROSS THE $Z = 0$ AXIS

ALPHA- 35
YAW - 0
ROLL - 0

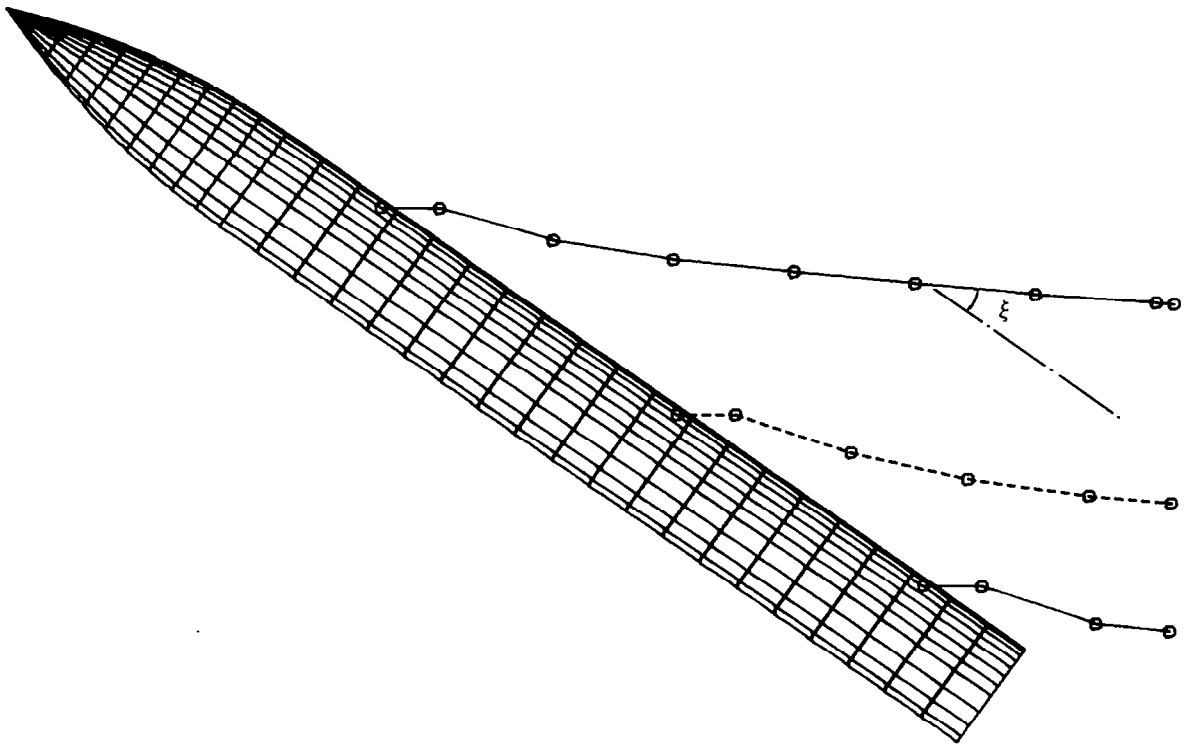


FIGURE 11. CURVED VORTEX MODEL APPLIED WITH 3 VORTICES
FOR 35° ANGLE OF ATTACK, VIEWED FROM THE SIDE.
THE ANGLE ξ IS INDICATED AT THE FIRST VORTEX.

ALPHA- 40
YAW - 0
ROLL - 1

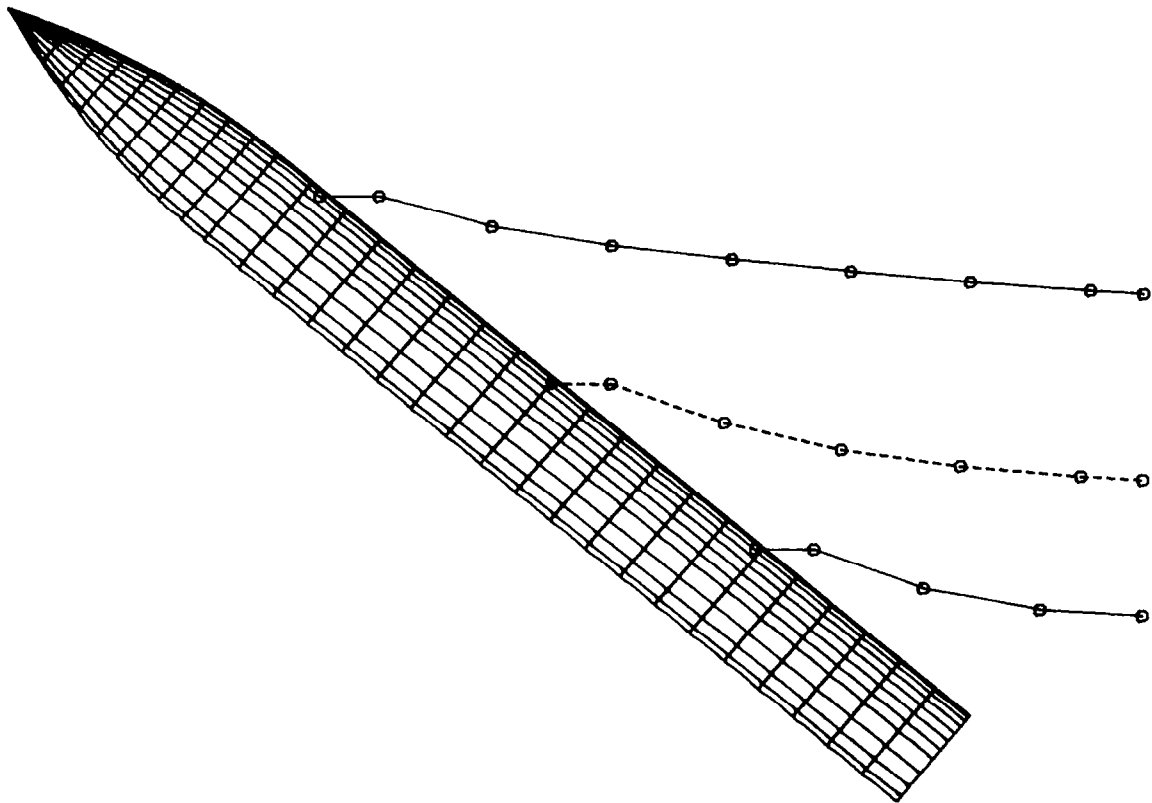


FIGURE 12. CURVED VORTEX MODEL APPLIED WITH 3 VORTICES
FOR 40° ANGLE OF ATTACK, VIEWED FROM THE SIDE.

ALPHA- 45
YAW - 0
ROLL - 0

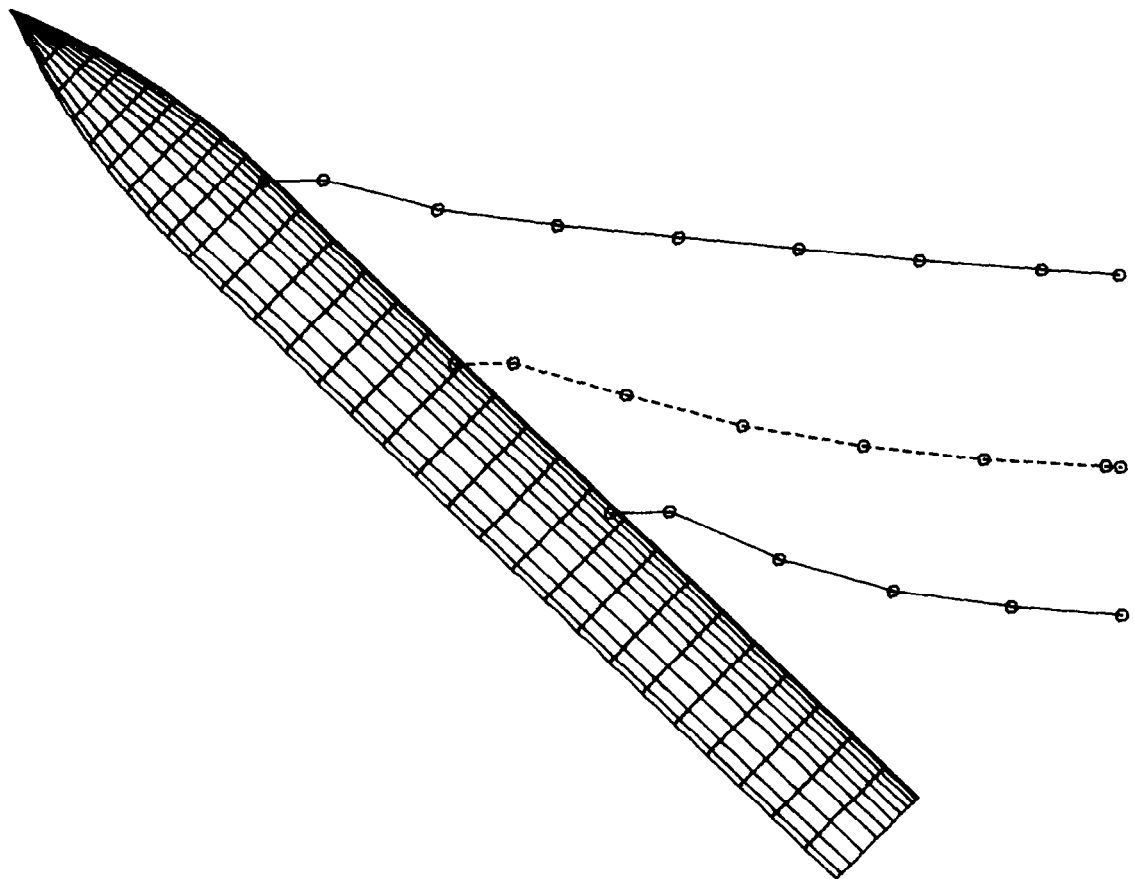


FIGURE 13. CURVED VORTEX MODEL APPLIED WITH 3 VORTICES
FOR 45° ANGLE OF ATTACK, VIEWED FROM THE SIDE.

ALPHA- 45
YAW - 0
ROLL - 0

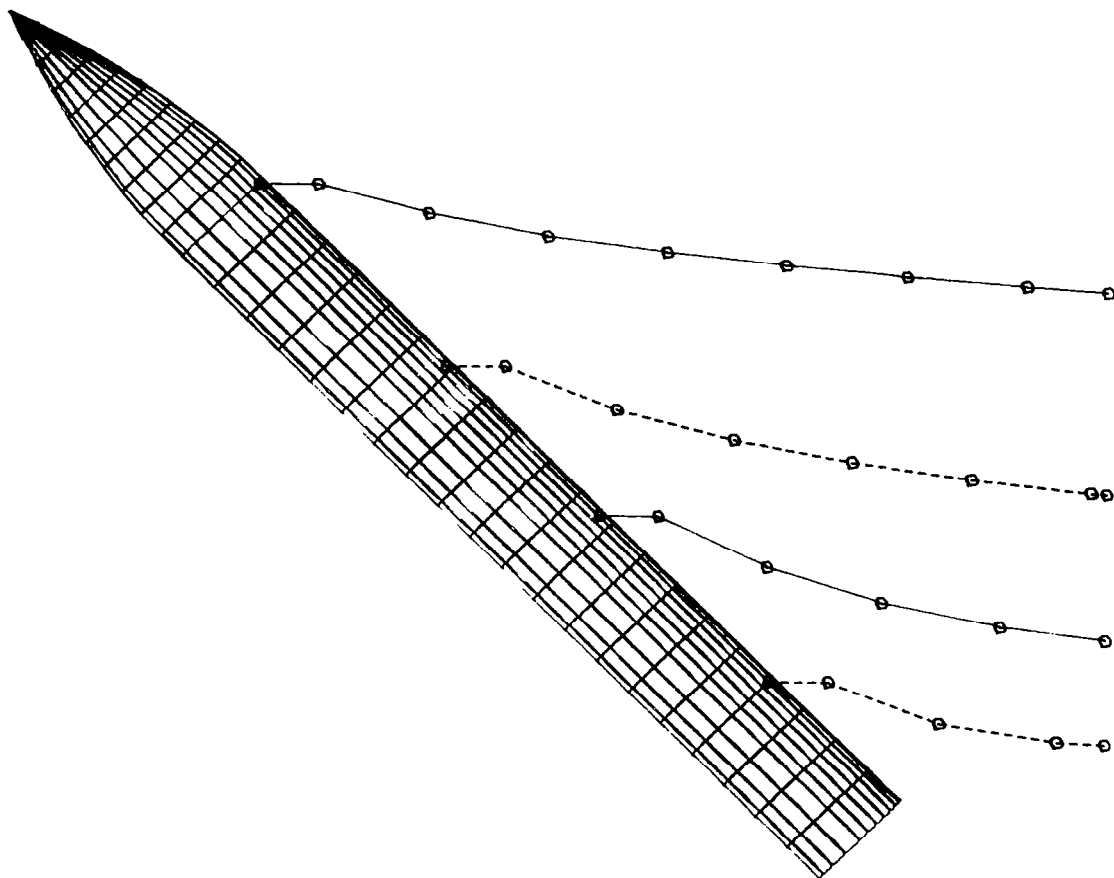


FIGURE 14. CURVED VORTEX MODEL APPLIED WITH 4 VORTICES
FOR 45° ANGLE OF ATTACK, VIEWED FROM THE SIDE.

ALPHA= 50
YAW - 0
ROLL - 0

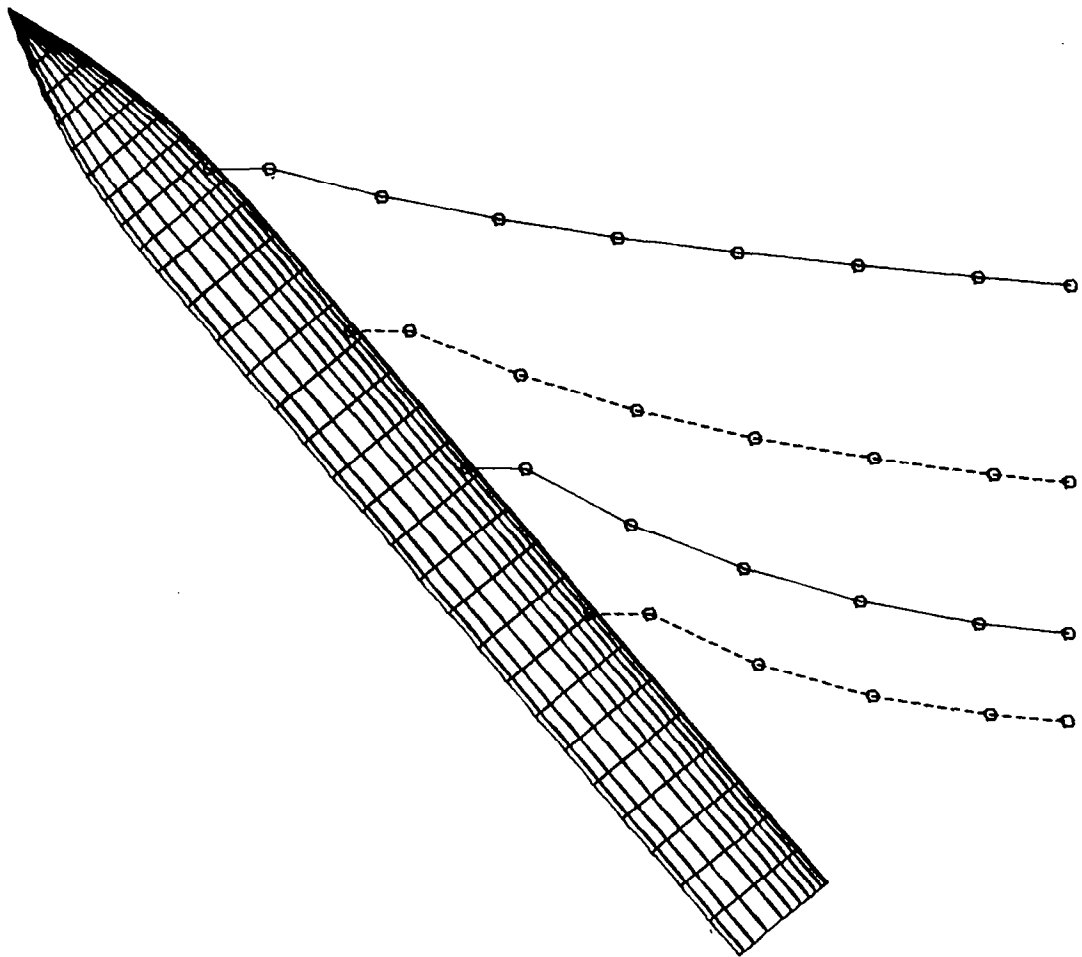


FIGURE 15. CURVED VORTEX MODEL APPLIED WITH 4 VORTICES
FOR 50° ANGLE OF ATTACK, VIEWED FROM THE SIDE.

ALPHA= 55
YAW - 0
ROLL - 0

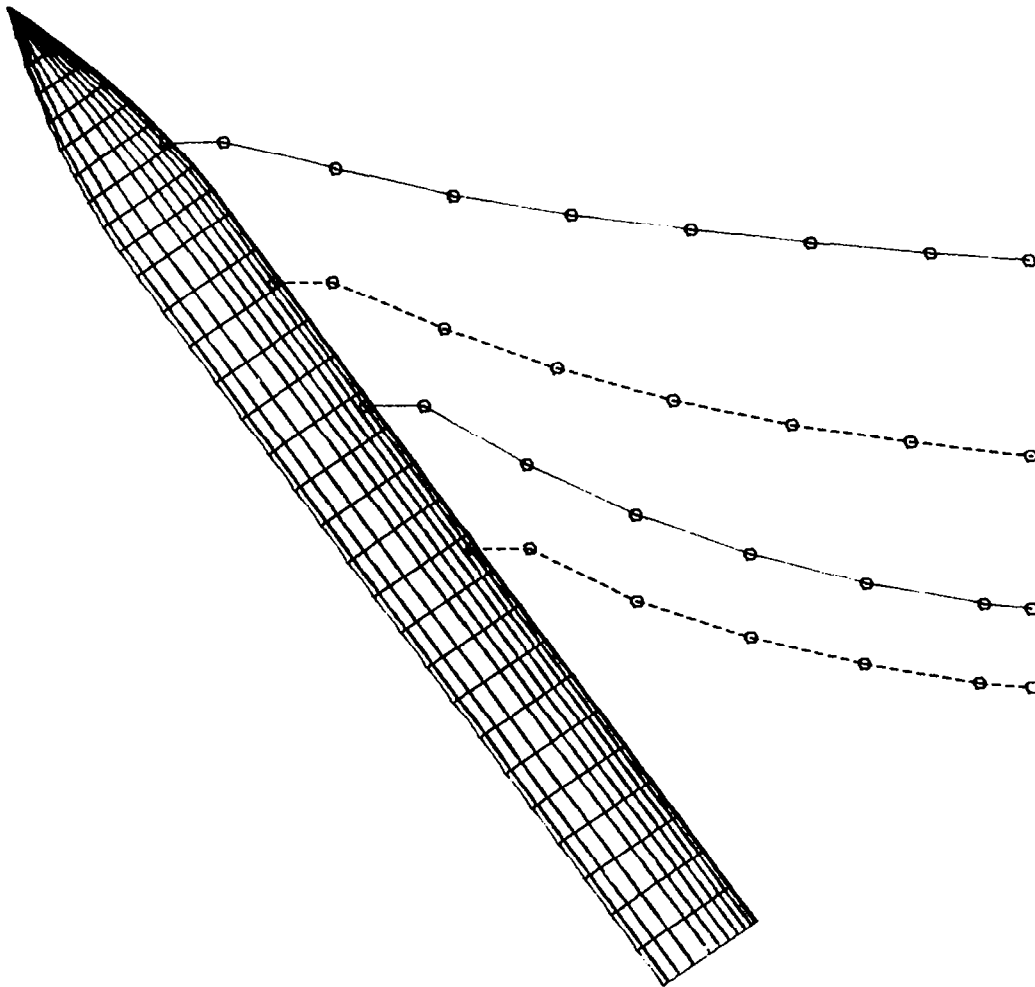


FIGURE 16. CURVED VORTEX MODEL APPLIED WITH 4 VORTICES
FOR 55° ANGLE OF ATTACK, VIEWED FROM THE SIDE.

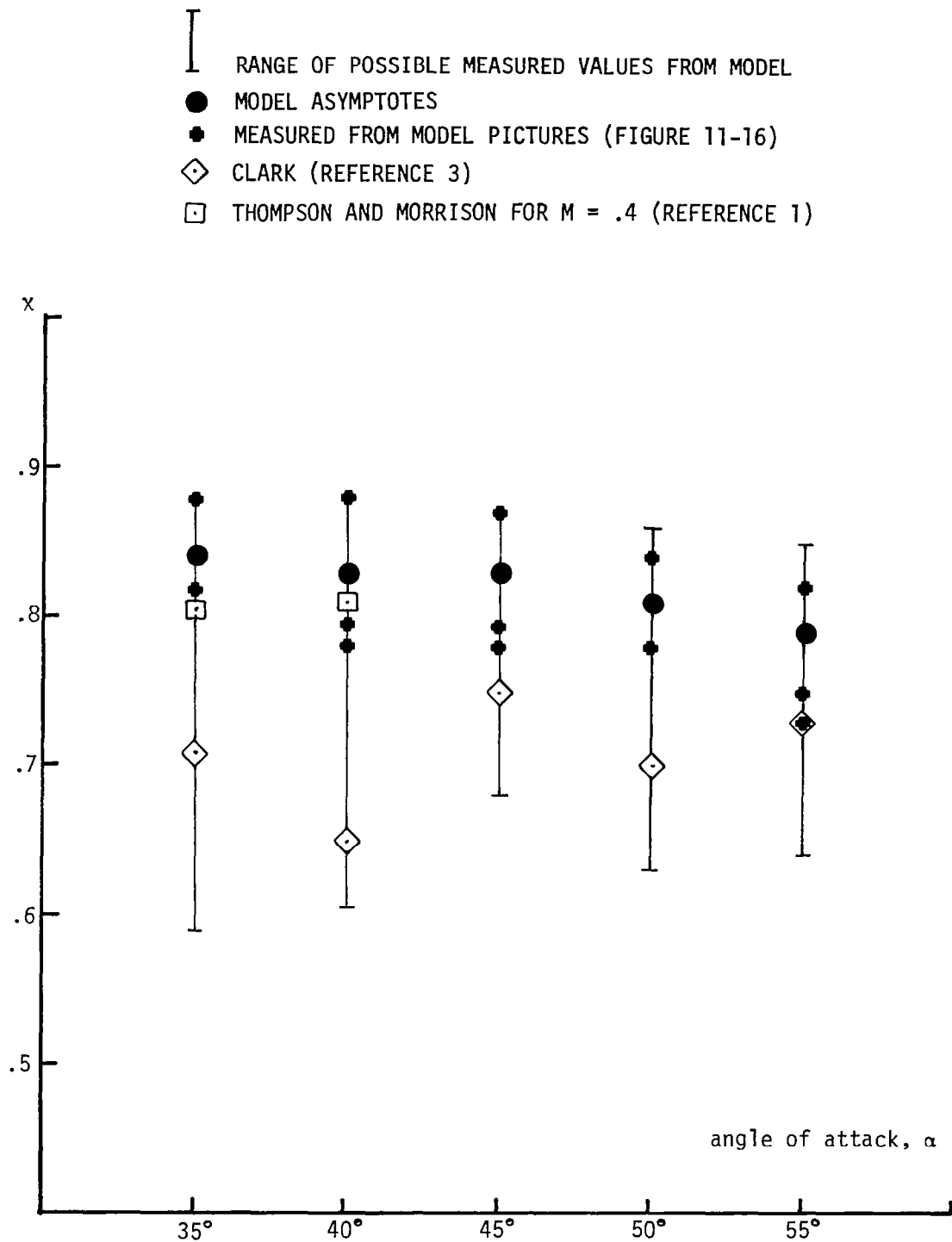


FIGURE 17. VARIATIONS OF $x = \tan \xi / \tan \alpha$ WITH ANGLE OF ATTACK

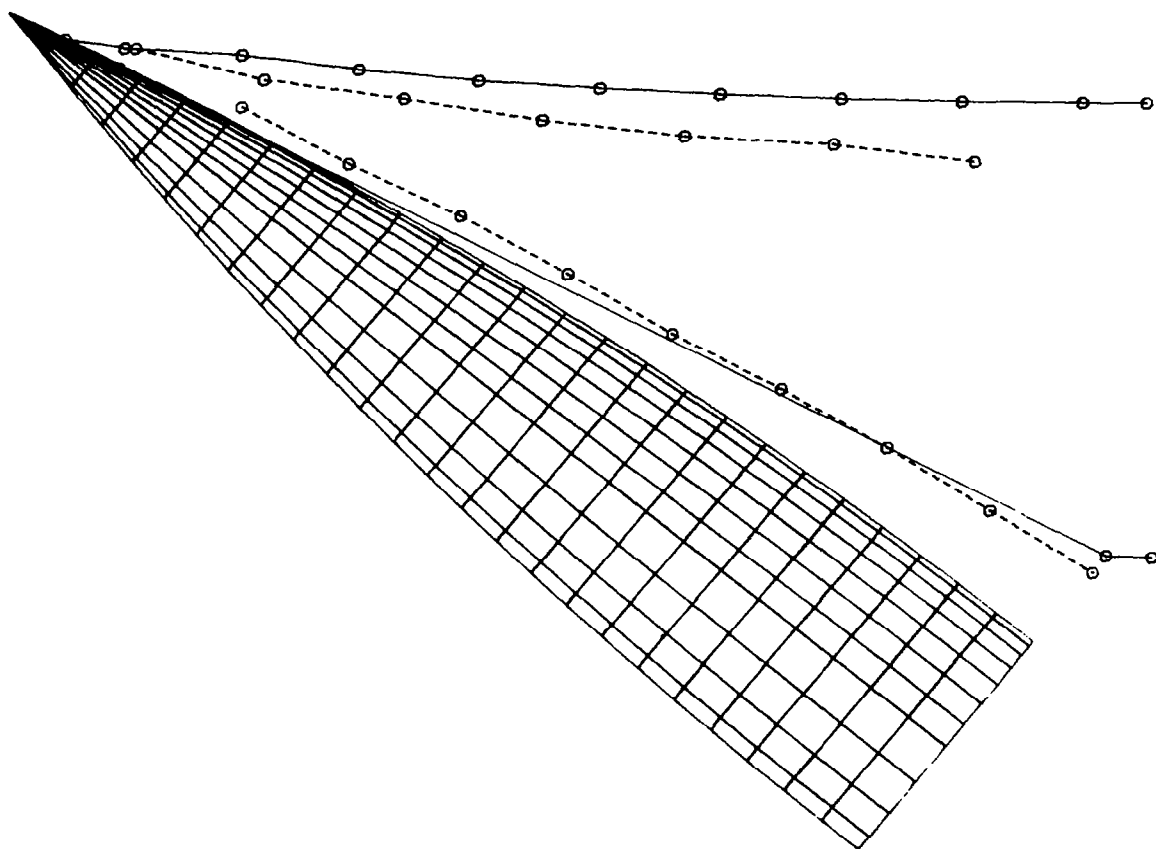


FIGURE 18. ELLIPTICAL OGIVE WITH MAJOR AXIS VERTICAL AT
 45° ANGLE OF ATTACK, VIEWED FROM THE SIDE.
 THE DASHED LINE CONNECTS THE MEASURED POSITIONS
 FROM REFERENCE 14.

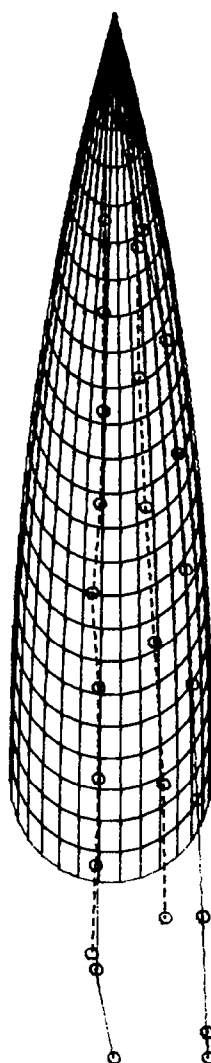


FIGURE 19. ELLIPTICAL OGIVE WITH MAJOR AXIS VERTICAL AT 45° ANGLE OF ATTACK, VIEWED FROM ABOVE. THE DASHED LINE CONNECTS THE MEASURED POSITIONS FROM REFERENCE 14.

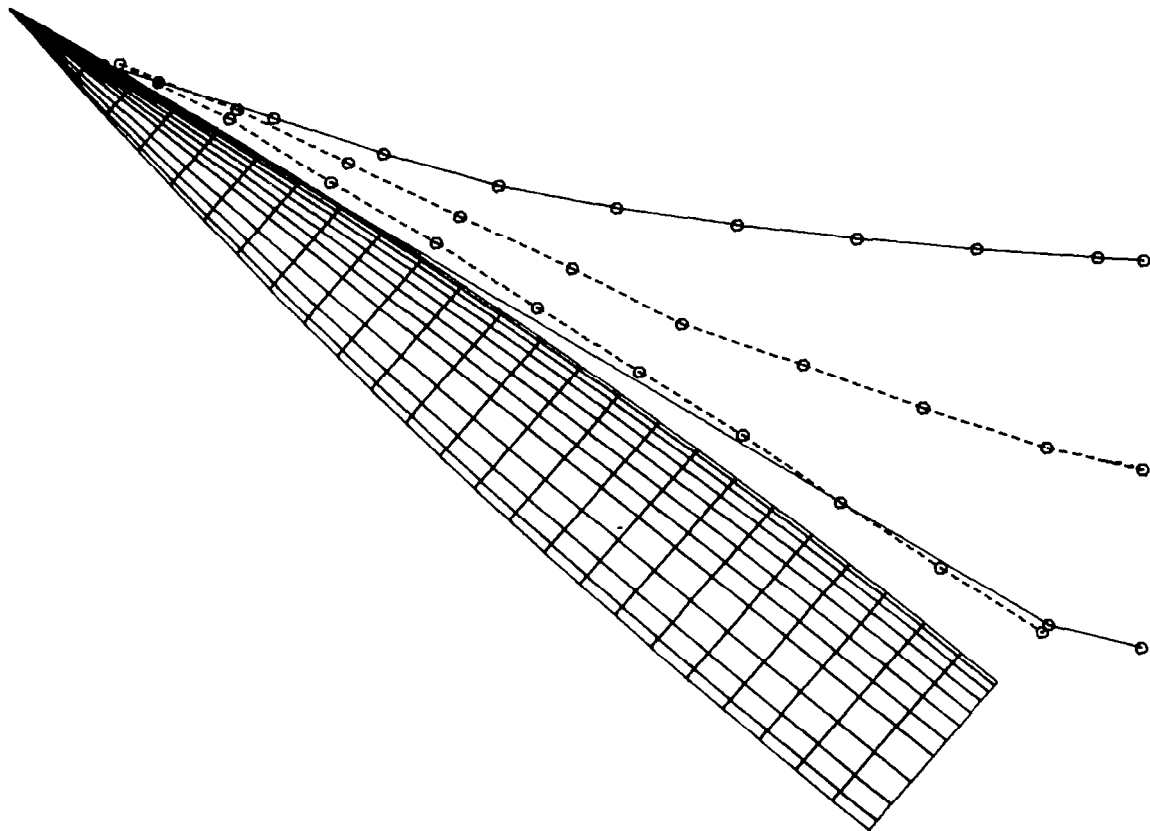


FIGURE 20. ELLIPTICAL OGIVE WITH MAJOR AXIS HORIZONTAL
AT 45° ANGLE OF ATTACK, VIEWED FROM THE SIDE.
THE DASHED LINE CONNECTS THE MEASURED POSITIONS
FROM REFERENCE 14.

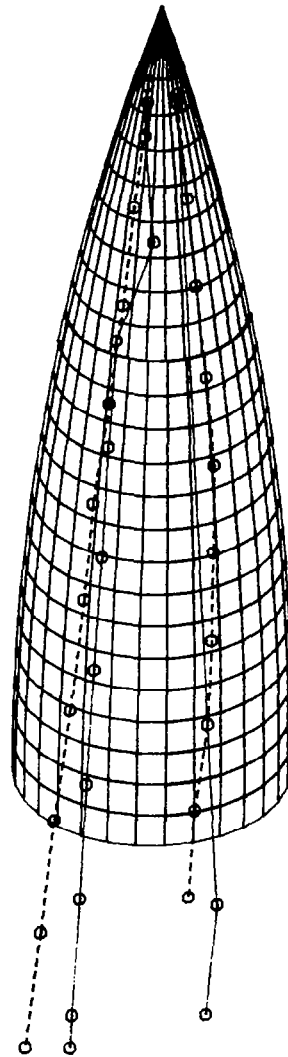


FIGURE 21. ELLIPTICAL OGIVE WITH MAJOR AXIS HORIZONTAL
AT 45° ANGLE OF ATTACK, VIEWED FROM ABOVE.
THE DASHED LINE CONNECTS THE MEASURED POSITIONS
FROM REFERENCE 14.

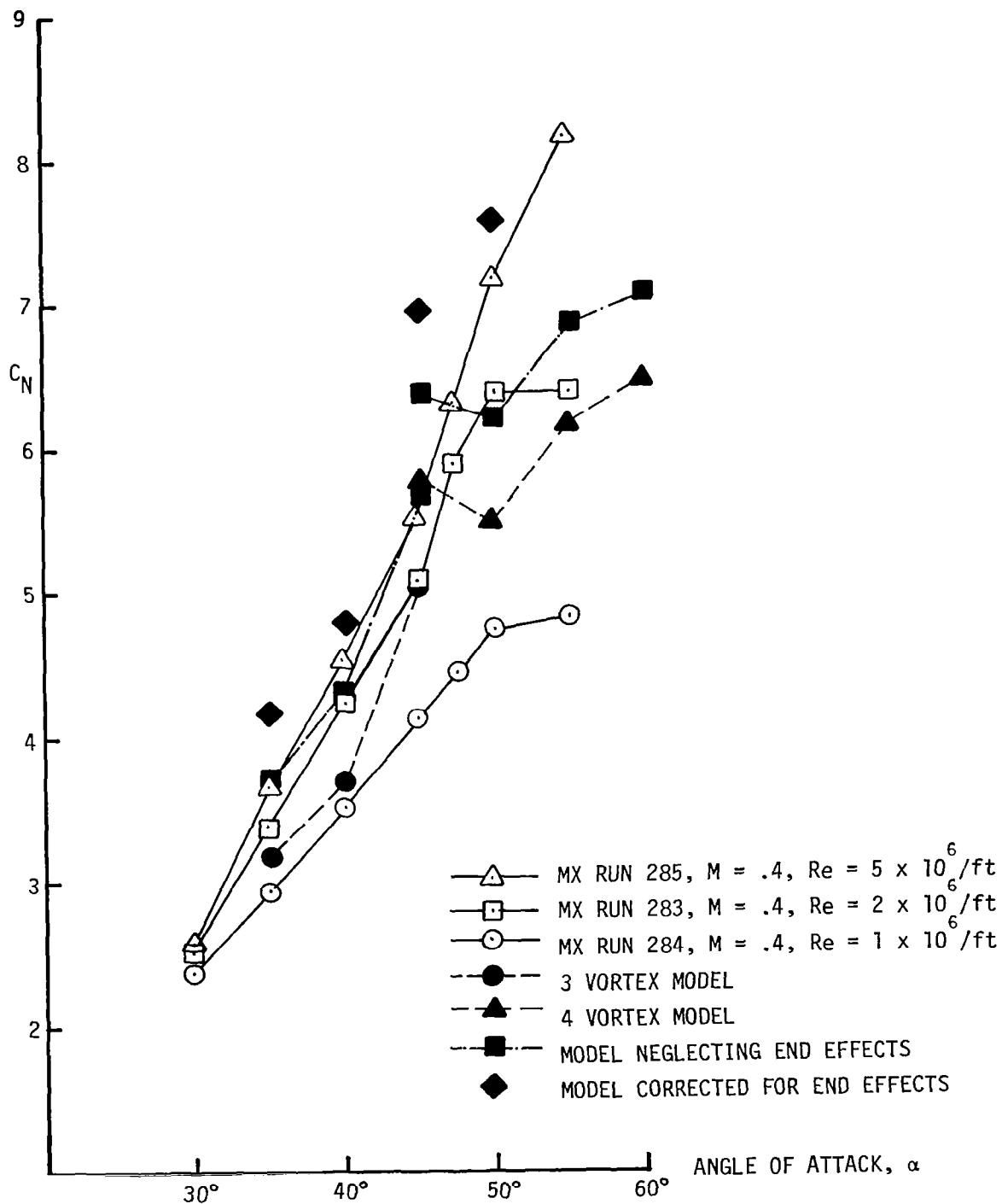


FIGURE 22. NORMAL FORCE VERSUS ANGLE OF ATTACK

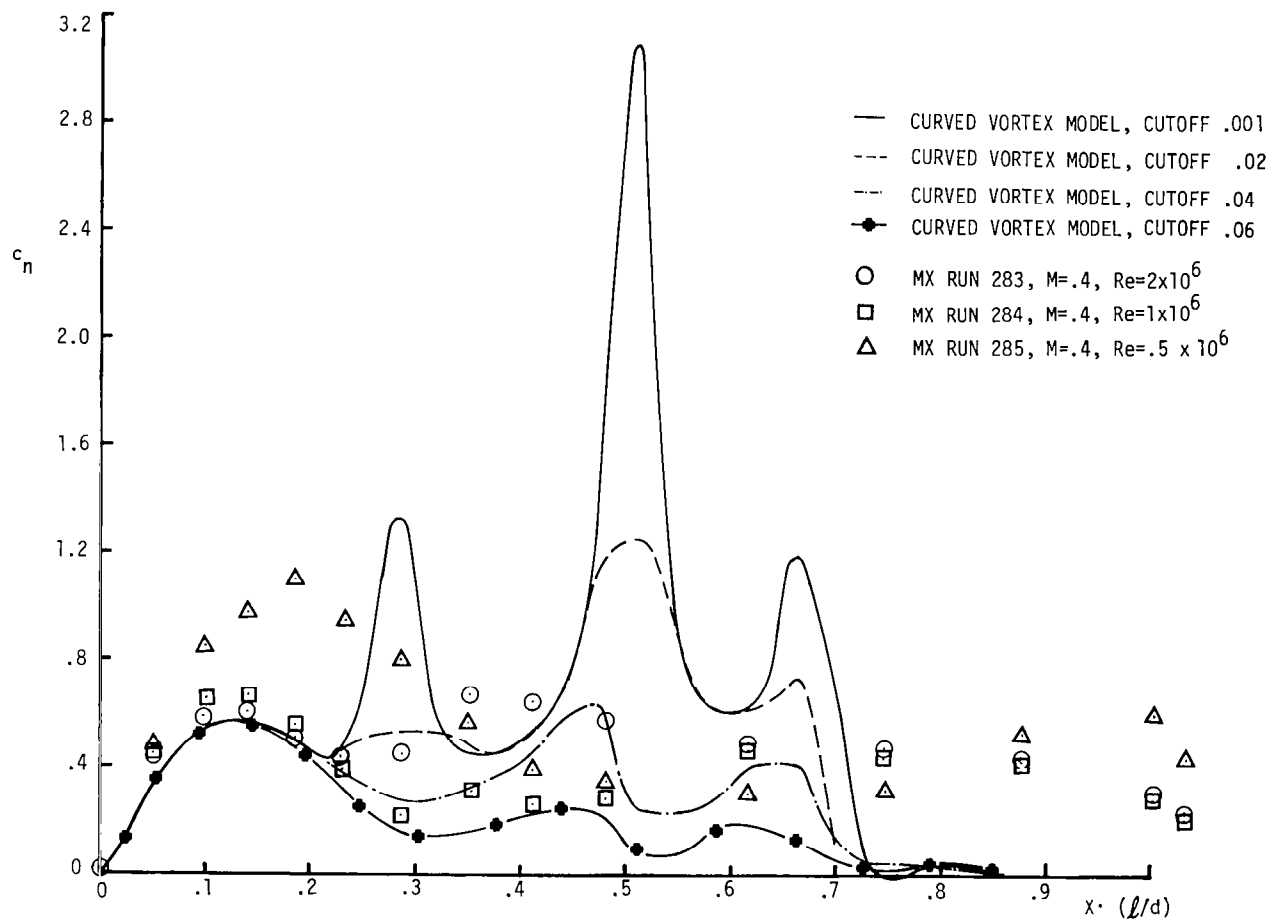


FIGURE 23. NORMAL LOAD DISTRIBUTION FOR SEVERAL VALUES OF THE CUTOFF PARAMETERS

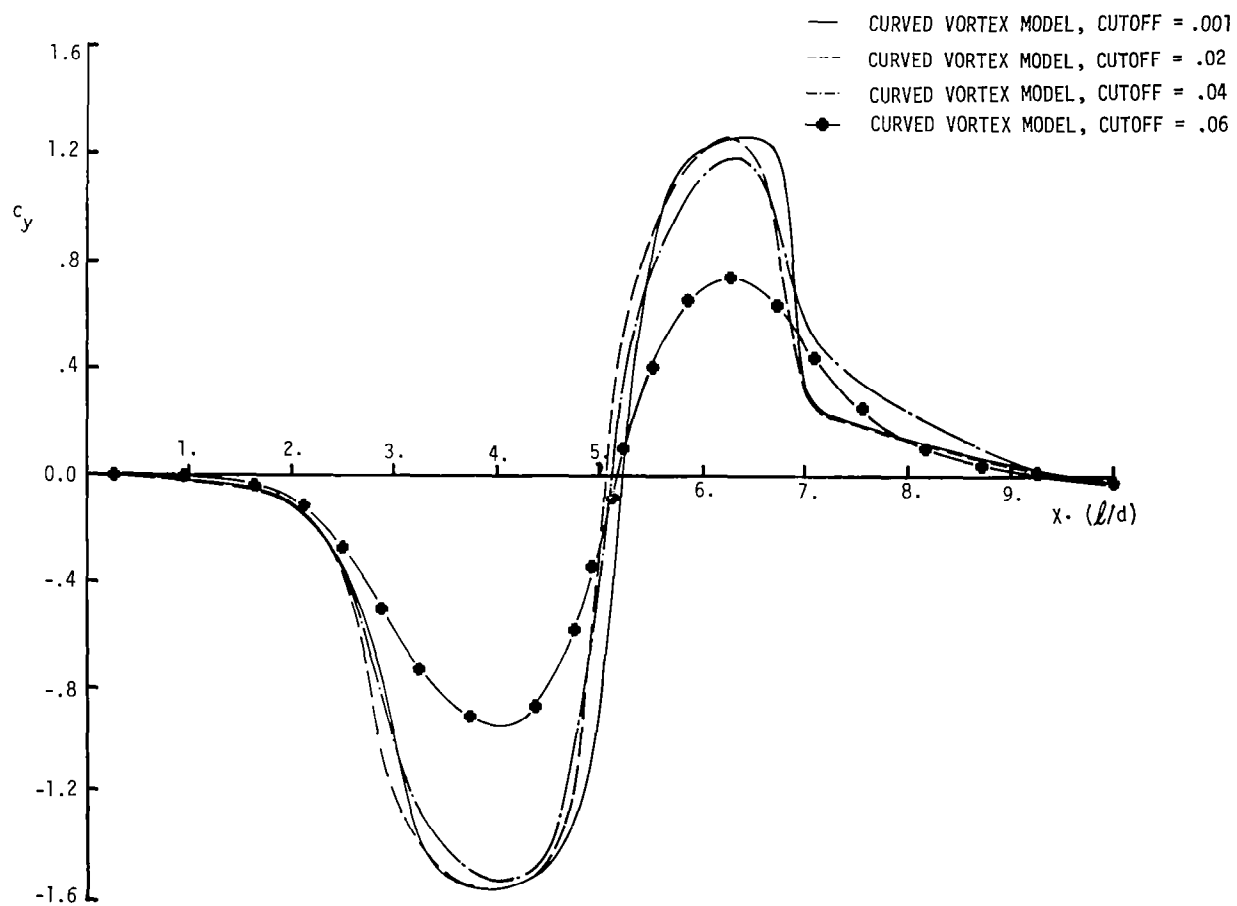


FIGURE 24. SIDE LOAD DISTRIBUTION AT 45° ANGLE OF ATTACK FOR VARIATION IN THE CUT OFF PARAMETER

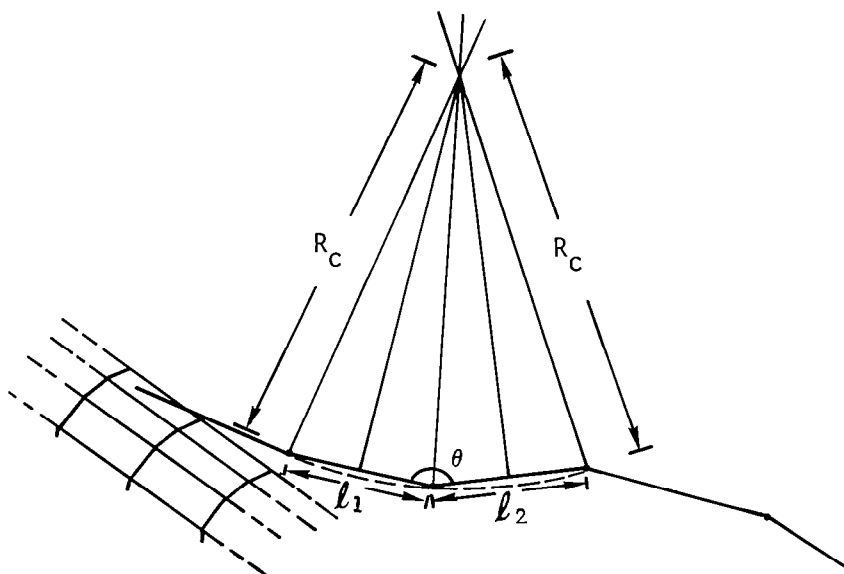


FIGURE 25. GEOMETRY FOR THE CALCULATION OF CURVATURE CONTRIBUTIONS IN THE CURVED VORTEX MODEL

1. Report No. NASA CR-3208		2. Government Accession No.		3. Recipient's Catalog No.	
4. Title and Subtitle A Three Dimensional Vortex Wake Model for Missiles at High Angles of Attack				5. Report Date January 1980	
				6. Performing Organization Code	
7. Author(s) J. Steven Sheffield F. D. Deffenbaugh				8. Performing Organization Report No. TRW Rep. #30584-6003-RU-00	
				10. Work Unit No.	
9. Performing Organization Name and Address TRW Defense and Space Systems Group One Space Park Redondo Beach, CA 90278				11. Contract or Grant No. NAS2-9579	
				13. Type of Report and Period Covered Contractor Report	
12. Sponsoring Agency Name and Address National Aeronautics and Space Administration Washington, D. C.				14. Sponsoring Agency Code	
15. Supplementary Notes Ames Technical Monitor: Gerald Malcolm					
16. Abstract <p>A three dimensional model for the steady flow past missile and aircraft nose shaped bodies is presented based on augmenting a potential solution with a wake composed of vortex filaments. The vortex positions are determined by the requirement that they in some sense align with the flow. The aerodynamic loads on the body are compared with experimental values and used to evaluate the model.</p> <p>The vortex positions compare well with flow visualization results for slender bodies at high angles of attack. The approximations in the wake near the body cause peaks in the force distributions more severe than in the measured values.</p> <p>For given vortex strengths and body attachment points multiple steady vortex positions were not found.</p>					
17. Key Words (Suggested by Author(s)) Vortex Filament Model High Angle of Attack Aerodynamics Missile Wake Three Dimensional Flow Field			18. Distribution Statement Unlimited Star Category - 02		
19. Security Classif. (of this report) Unclassified		20. Security Classif. (of this page) Unclassified		21. No. of Pages 53	
				22. Price* \$5.25	